

24

25 **Abstract**

26 Increasing climatic variability has resulted in an unprecedented surge in extreme events,
27 pressing global ecosystems towards systematic breakdown. Yet, the resilience of the soil-
28 vegetation-atmosphere (SVA) system to revert to its natural state indicates the existence of
29 energetic barriers forbidding systems from tipping. Observational and theoretical constraints limit
30 our understanding of these energetic barriers which are crucial for assessing ecosystem sensitivity
31 to atmospheric perturbations. We provide a novel coherent theory on the dissipative energy
32 barriers (Δe) which decides the resilience potential of an ecosystem. These barriers are
33 manifestation of lower bounds of entropy produced (Σ^*) for unit anomaly transference from soil
34 moisture (SM) to evapotranspiration (ET). Using remote sensing data, we compute these global
35 entropy bounds by introducing a new metric (Wasserstein distance, d_W) for SM-ET coupling.
36 Quantifying these lower bounds from SM-ET coupling, places terrestrial ecosystems in the
37 hierarchy of dissipative energy states spanning from forested regions to barren lands. Furthermore,
38 we show that the optimization of SM-ET coupling translates to entanglement of water potential
39 gradient ($\Delta\omega$) between land surface and atmospheric boundary layer, and the resulting memory
40 timescale or residence time (τ). This ($\tau\Delta\omega$) entanglement propels moisture-rich and moisture-
41 deficit systems in complementary evolutionary pathways in responding to imposed anomalies. As
42 a result, we witness an emergence of coupling-aridity tradeoff with temperate climates operating
43 as least efficient systems for unit SM to ET anomaly transfer. Physical basis, and transferability
44 across space and scale makes this theory a potential benchmark for process improvement in the
45 climate and earth system models.

46

47

48 **Plain Language Summary**

49 In recent years, extreme events have put a lot of pressure on the planet's ecosystems, but
50 they seem to have a natural ability to bounce back. However, a fully developed mechanical
51 understanding of these energy barriers that stop these systems from tipping is lacking. We argue
52 that the effects of atmospheric disturbances on land surfaces can be comprehended from their
53 interaction through signatures in soil moisture (SM) – evapotranspiration (ET) coupling. Hence,
54 quantifying the entropy thresholds for unit anomaly transfer from SM to ET can provide new
55 means for computing the resilience of ecosystems. Using an optimization framework, it is shown
56 that the driving water potential ($\Delta\omega$) and memory timescale (τ) of moisture anomalies are
57 entangled. This has repercussions on how global hydroclimates cope up with varied level of
58 atmospheric dryness. This theory could be a useful tool for improving climate and Earth system
59 models because it's based on physical principles and can be applied to different places and scales.

60

61

62 **I. Introduction**

63 Recent years have witnessed a surge in weather-related extremes across the globe, boosting
64 the “dry getting dryer, and wet getting wetter” paradigm over the majority of terrestrial landscapes
65 (Dosio et al., 2018; Perkins-Kirkpatrick & Lewis, 2020). Comprehending the land surface
66 responses to these atmospheric perturbations has thus become of increasing significance, for
67 improving climate forecasts and predicting ecosystem resilience (Sehgal et al., 2021; Verbesselt
68 et al., 2016). The coupled terrestrial water-energy system entails signatures from these continuous
69 atmospheric perturbations, the imprints of which are registered in soil-vegetation response through

70 changes in soil moisture (SM) - evapotranspiration (ET) coupling (Dirmeyer, 2011; Koster et al.,
71 2004; Seneviratne et al., 2006). Intricately connected to SM-ET coupling is the concept of memory
72 timescale (τ), defined as the time needed by a land unit to forget an imposed anomaly (Koster &
73 Suarez, 2001; McColl et al., 2017). Conventionally, τ has been quantified using the autocorrelation
74 of SM time series with previous literature observing similar timescales under spatially distinct
75 regions of the world (Ghannam et al., 2016; McColl et al., 2019; Teuling et al., 2006). Given the
76 importance τ plays in modulating land-atmospheric feedback, such overlapping results provokes a
77 deeper question of whether a unifying governing principle underlies these empirically observed
78 timescales, and if so, to what extent does the presence of such a principle impact the dynamics of
79 terrestrial water-energy interactions?

80 As soil moisture evaporation (and transpiration through plants) involves irreversible heat
81 and mass transfer, thermodynamics serves as a universal means to declutter SM-ET coupling
82 dynamism from an energy perspective. A continuous atmospheric circulation maintains water
83 potential gradient and results in sustained entropy production through SM-ET conversion
84 (Kleidon, 2008). The presence of water potential gradient also signifies non-equilibrium (NE)
85 state, and the maximum entropy production (MEP) principle states that system in NE will adapt to
86 *steady states* at which they dissipate energy and produce entropy at the maximum possible rate
87 (Kleidon, 2010). Under such conditions, the rate of change in SM and ET approaches a nearly
88 constant value inherent to the system (Kleidon, 2010), defined here as *non-equilibrium steady state*
89 (NESS), and characterized by nonzero fluxes and nonzero potential gradients (Qian, 2006). Hence,
90 entropy production quantifies how much a physical system is driven away from equilibrium by
91 capturing a system's evolution (in this case SM-ET coupling) in response to the environment.

92 From a systems perspective, a hydroclimate can be thought of as a particular configuration
93 of soil-vegetation-atmosphere (SVA) characterized by long-term *expected* behavior in process
94 interactions constrained upon energy fluxes in and out of the system. Responses of SVA systems
95 to changes in atmospheric forcings are dependent on the nonlinear relationship between energy
96 fluxes and soil moisture (Feldman et al., 2022). Nevertheless, when supported by soil hydrological
97 processes (SHP) in modulating the impact of atmospheric perturbations, hydroclimates across the
98 globe often demonstrate the tendency to return back pre-anomaly conditions - described as
99 *resilience* of the system in previous literatures (Berdugo et al., 2020; Fu et al., 2022; Verbesselt et
100 al., 2016). This is evident from responses displayed by most systems to frequent and seasonal
101 atmospheric perturbations within meteorological (and often climatic) time scales through gradual
102 recovery to optimum NESS. Hence, resilience can be considered the tendency of SVA to *hold-on*
103 to NESS, unique to a SVA configuration. We hypothesize that the resilience of any SVA to
104 maintain its configuration in a preferred NESS is compensated by paying through equivalent
105 entropy production. Hence, any change in SVA will be induced through changes in entropy
106 production and preferred NESS.

107 However, with changing climate, the modulating capacity of SHP are severely impacted
108 (Seneviratne et al., 2006; Vereecken et al., 2022) rendering a higher probability for the system's
109 threshold to be crossed and making the system vulnerable to topple into a new stable state with
110 different NESS (Berdugo et al., 2020). Therefore, it becomes critical to quantify these lower
111 bounds of the entropy barrier which when crossed will alter the climate to a new stable state
112 defining transitions between hydroclimates. Statistical physics literature has delved into the
113 explainability of optimal control of stochastic thermodynamic systems using optimal transport
114 (OT) theory (Benamou & Brenier, 2000; Dechant, 2022; Dechant & Sakurai, 2019; Nakazato &

115 Ito, 2021; Van Vu & Saito, 2022). OT concerns the means by which one can optimally transport a
116 source distribution to a target distribution, characterized by a metric called the Wasserstein
117 distance (d_W) (Dechant & Sakurai, 2019; Van Vu & Saito, 2022). Studies have shown that for a
118 stochastic process, the lower bound of entropy production could be expressed as a function of d_W
119 between the initial and final states of the system's distribution (Dechant, 2022). We adapt d_W as
120 the coupling metric and derive the expression for lower bound of entropy production in SM-ET
121 transitioning, with water moving from soil to atmosphere or soil to plant to atmosphere.
122 Furthermore, using equivalence between statistical and classical thermodynamics, we show that
123 the optimization of SM-ET coupling transcends to the entanglement of the water potential gradient
124 ($\Delta\omega$) which drives the moisture out of the system and the resulting memory timescale (τ), or
125 residence time across root water uptake to stomatal expulsion.

126 In this study, we aim to answer a key question: When there's an exchange of anomalies
127 from soil moisture (SM) to evapotranspiration (ET), what is the minimum memory timescale and
128 entropy production required for this process? To achieve this, the paper addresses three primary
129 objectives: (1) determine the minimum levels of entropy production needed for various global
130 hydroclimates for unit anomaly transference, (2) establish a fundamental relationship between the
131 strength of the coupling between SM and ET and the memory timescale, and (3) investigate the
132 evolutionary paths taken by climatic systems that adhere to these proposed optimization principles.
133 Additionally, we develop a coherent theory concerning the resilience of ecosystems by introducing
134 the concept of dissipative energy barriers (DEB), which are derived from entropic thresholds at
135 which a system operates.

136 **2. Data Set**

137 ***2.1 Satellite SM and ET Datasets***

138 Combined (active + passive) surface soil moisture (SSM) data (Lopez, 2018) provided by
139 Copernicus Climate Change Service (C3S) for the period Jan 2010 – Dec 2019 was used for the
140 analysis. The product is gridded at $0.25^\circ \times 0.25^\circ$ spatial and 1 day temporal resolution, and captures
141 the top few centimeters of the soil where the land-atmosphere mass exchanges and biological
142 processes for plant growth are concentrated (Ouedraogo et al., 2013). Supplementary Table S1
143 outlines the sensors used for producing the combined product. Recent studies have shown that
144 surface moisture carries information about deeper profiles beyond the generally attested top 5cm
145 (Short Gianotti et al., 2019) and can inform about evapotranspiration regime changes (Dong et al.,
146 2022). To avoid ambiguity, we will denote surface moisture as SM.

147 For evapotranspiration (ET), the gap-filled product from Terra MODIS (i.e.,
148 MOD16A2GF) for the period 2010-2019 was used for the analysis (Running et al., 2019). It is
149 based on the Penman-Monteith equation and is available at 500 m spatial resolution and temporally
150 as 8-day composite i.e., pixel values are the sum of all eight days within the composite period.

151 ***2.2 Ancillary Datasets***

152 Water - Energy clustering (WEC) classification proposed by Pisarello & Jawitz (2021)
153 were used for global hydroclimate reference owing to its inclusion of ET into the classification
154 scheme. The 15 WEC zones were resampled into five primary groups based on increasing zone
155 mean aridity index ($\phi = \text{Potential Evapotranspiration (PET)}/\text{Precipitation (P)}$), namely Super
156 Humid ($\phi = 0.39$), Humid ($\phi = 0.58$), Temperate ($\phi = 1.07$), Arid ($\phi = 2.05$), and Hyper Arid ($\phi =$
157 9.56). MODIS Annual International Geosphere-Biosphere Program (IGBP) classification (Sulla-
158 Menashe et al., 2019) was used for ecosystem classification. We broadly categorize them into
159 forests (F), savannahs (SV), croplands (CRP), grasslands (GR), shrublands (SH), and barren land
160 (B). Bias corrected ERA5 reanalysis meteorological and soil temperature datasets (supplementary

161 Table S2) were used for computation for near surface boundary layer chemical water potential and
 162 entropy production. van Genuchten soil water characteristics (SWC) and saturated hydraulic
 163 conductivity parameters provided in (Gupta et al., 2020, 2022) were used along with vegetation
 164 hydraulic parameters provided in Liu et al. (2021) for soil and vegetation matric potential
 165 calculation, respectively. MODIS NDVI (Didan, 2015) data was used for vegetation water content
 166 calculation. Canopy height derived from sentinel-2 images (Lang et al., 2022) were used as proxy
 167 for travel length for water particles.

168 All datasets were linearly rescaled to $0.25^\circ \times 0.25^\circ$ spatial resolution (hereon referred as
 169 *footprint* scale) through bilinear interpolation and spaced at 8-day temporal resolution in
 170 accordance with MODIS ET retrieval dates. Ancillary datasets were spatially resampled to match
 171 the extents of SM and ET raster's and averaged over four seasons (MAM - March through May,
 172 JJA - June through July, SON - September through November, DJF - December through February).
 173 Data processing and analyses were done in the R environment (RStudio 2022.12.0+353), and
 174 optimal transport calculations were performed using the transport library (Schuhmacher et al.,
 175 2022).

176 **3. Methodology**

177 ***3.1 Unit anomaly transference and Non-Equilibrium Steady State (NESS)***

178 A variety of micro-scale mechanisms govern flow transport and SM-ET coupling, and
 179 describing their footprint scale manifestation requires generalization of the representative
 180 dominant processes (also termed as “*effective*” processes) keeping the pore-scale physical
 181 description intact (Blöschl & Sivapalan, 1995; Crow et al., 2012; Mohanty, 2013; H. Vereecken
 182 et al., 2007). Utilizing the fundamental mass balance and phase change kinetics, Ouedraogo et al.,
 183 (2013) described a non-equilibrium model for water transport (equation 1 and 2),

184 $\frac{\partial \rho_l}{\partial t} + \nabla \cdot (\rho_l v_l) = -\widehat{\rho}_v$ (1)

185 $\frac{\partial \rho_v}{\partial t} + \nabla \cdot (J_v) = \widehat{\rho}_v$ (2)

186 where ρ_l and ρ_v (kg m^{-3}) are the apparent density of soil water and its vapor respectively, v_l (m
 187 s^{-1}) is the soil water flux, J_v ($\text{kg m}^{-2} \text{s}^{-1}$) is the vapor diffusion flux, and $\widehat{\rho}_v$ ($\text{kg m}^{-3} \text{s}^{-1}$) is the
 188 phase-change rate. Assuming a strong degree of coordination between liquid and vapor phase
 189 water transport (Katul et al., 2012), the soil-plant hydrodynamics for vertical water motion on a
 190 footprint scale, equation (1) and (2) can be combined to form a generalized continuity equation
 191 described in terms of effective diffusion flux,

192 $\frac{\partial \rho_{eff}}{\partial t} + \nabla \cdot (J_{eff}) = 0$ (3)

193 where ρ_{eff} ($= \rho_l + \rho_v$) is the effective density of liquid water and vapor, and J_{eff} ($= \rho_l v_l + J_v$) is
 194 the effective diffusion flux resulting from effective velocity field $v_{eff}(x)$ which is a function of
 195 both time t and position x of the particle undergoing diffusion. Here, effective velocity describes
 196 the net directional movement of water molecules with which they are transported through soil-
 197 vegetation continuum during ET. Many experimental studies on evaporation in porous media have
 198 suggested the dominance of vapor flow near the surface (~ 20 to 100 mm) (Brutsaert, 2014;
 199 Lehmann et al., 2008; Shokri et al., 2009). As such for footprint observations of surface retrievals,
 200 we assume SM-ET anomaly transference (water transport) to be dominated by diffusive fluxes and
 201 an instantaneous phase change. The rate of change of these transport fluxes can be described in
 202 terms of NESS, defined as the section of the dynamic regime where SVA spends most of its time,
 203 and mathematically represented as the mode of the distribution,

204 $NESS_x = \lim_{\Delta(\frac{x_{t_j} - x_{t_i}}{t_j - t_i}) \rightarrow c} \frac{x_{t_j} - x_{t_i}}{t_j - t_i}$ (4)

205 where X_{t_i} and X_{t_j} are successive observations at time t_i and t_j . Here the limit reflects the slowing
 206 down in rate of change to a steadier value c in the neighborhood of 0 – function of soil and
 207 vegetation type. Thus, NESS represents the coherent macroscopic ensemble of the SM and ET at
 208 footprint scale. For application of OT, $NESS_{SM}$ and $NESS_{ET}$ are expressed in the same
 209 configuration space using a dimensionless quantity called the Anomaly Impact Factor (AIF),
 210 defined as the ratio of rate of change of variable at incremental time steps divided by its long-term
 211 standard deviation σ ,

$$212 \quad AIF_X = \frac{\left(\frac{X_{t_j} - X_{t_i}}{t_j - t_i}\right)}{\sigma \left(\frac{X_{t_j} - X_{t_i}}{t_j - t_i}\right)} \quad (5)$$

213 AIF configuration space (Fig. 1) displays the transformation of SM anomalies distribution to ET
 214 anomalies distribution through an OT framework and provides an advantage of envisioning SM-
 215 ET coupling from a disturbance propagation point of view.

216 **3.2 Optimal Transport Framework for SM-ET coupling**

217 Evolution, when stated in terms of statistical physics, is probable motion (Kaila & Annala,
 218 2008). OT provides a linkage between time evolution of probability density of a diffusing particle
 219 and associated entropy production through an analogy to least work done (energy optimum) by the
 220 system. We consider the distance cost function $c(x,y)$ of transporting a single water particle at the
 221 point $x \in SM_{AIF}$ to the point $y \in ET_{AIF}$, both defined on AIF configuration space (Fig. 1). Our aim
 222 is to minimize $c(x,y)$ subject to all possible paths of transferring the particle from SM_{AIF}
 223 distribution (say $s(x)$) to ET_{AIF} distribution (say $e(y)$). According to Monge-Kantrovich (MG)
 224 minimization problem, the optimal transport cost for $c(x,y)$ between two probability distributions
 225 $s(x)$ and $e(y)$ is defined as

$$226 \quad C(s, e) = \min_{\pi \in \delta(s, e)} \int c(x, y) \pi(x, y) dx dy \quad (6)$$

227 where the lower bound is taken over the entire set $\delta(s, e)$ of joint probability distributions $\pi(x, y)$
 228 whose marginal distributions are $s(x)$ and $e(y)$, i.e.,

$$229 \quad \delta(s, e) = \left\{ \begin{array}{l} \pi|s(x) = \int \pi(x, y)dy, \\ e(y) = \int \pi(x, y)dx \end{array} \right\} \quad (7)$$

230 s.t. $\pi(x, y) \geq 0$

231

232 Hence, the optimal transport cost gives a minimum of the expected value of the cost $c(x, y)$

233 for the joint distribution $\pi(x, y)$, also referred to as the optimal transport plan (Nakazato & Ito,

234 2021). Considering L^2 norm as the optimal transport cost on the AIF space leads to the $L^2 - d_W$.

235 Explicitly, the $L^2 - d_W$ between s and e is defined as

$$236 \quad d_W(s, e)^2 = \min_{\pi \in \omega(s, e)} \int ||x - y||^2 \pi(x, y) dx dy \quad (8)$$

237 which is equivalent to optimal transport cost $C(s, e)$ for the cost function $c(x, y) = ||x - y||^2$.

238 Thus, d_W as an optimal coupling measure quantifies the Euclidean length-scale for transferring a

239 unit anomaly from SM_{AIF} to ET_{AIF} . A low d_W indicates immediate coupling, while a larger d_W

240 indicates delayed coupling (Fig 1). Here on, d_W will mean $L^2 - d_W$ and $d_W(s, e)^2$ will be

241 represented as d_W^2 in short.

242 **3.3 A Comprehensive SM-ET coupling framework**

243 Owing to the critical role played by SM-ET coupling, the topic has received a lot of

244 attention over the years with studies often suggesting contrasting results for similar regions (Koster

245 et al., 2004; Seneviratne et al., 2010; Tuttle & Salvucci, 2016). The discrepancies in previous

246 coupling studies stems primarily from the methodology applied (modeled versus observation

247 based) and corresponding perception of terminologies (positive versus negative coupling, strong

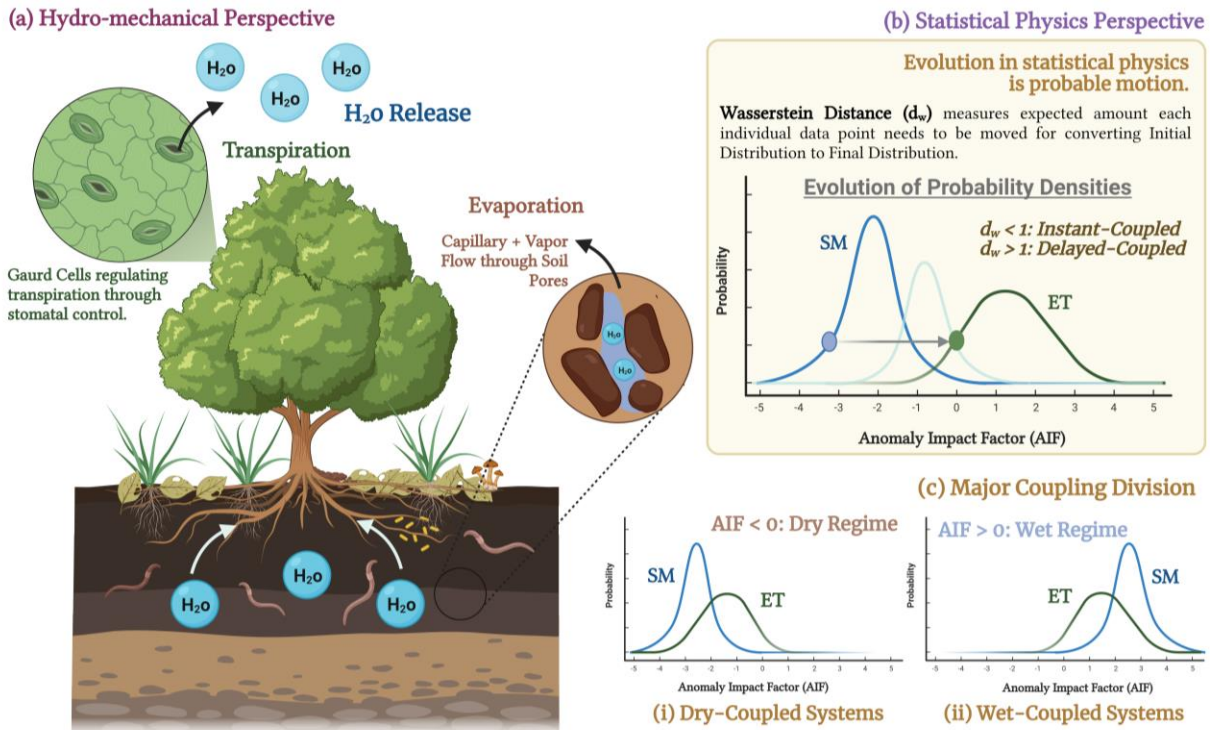
248 versus weak coupling). Here we propose a more comprehensive division of SM-ET coupling (Fig.

249 1) starting with a broader segmentation into (a) *instant (or immediate) coupling* ($d_W < 1$), and (b)

250 *delayed (or deferred) coupling* ($d_w > 1$). The instant coupled systems are further branched into
251 (a) *dry-coupled* ($AIF < 0$), and (b) *wet-coupled* ($AIF > 0$) systems. Dry-coupled systems are regions
252 which preferentially stay in dry regime (and SM limited) for both SM and ET (for example, arid
253 and hyper arid regions). These dry-coupled systems are predominantly demand-driven, i.e., a high
254 vapor pressure deficit allows for quicker transference of anomalies referred to as pulse reserve
255 mechanism in previous literature (Feldman et al., 2018). On the other extreme are wet-coupled
256 systems demarcating regions with wet regime preferences (for example humid and super humid
257 regions). These systems are primarily supply-driven, i.e., a relatively higher SM replenishment
258 maintains continuous infusion of moisture into the atmosphere. These systems have higher moist
259 static energy (Eltahir, 1998).

260 In between the dry-coupled and wet-coupled systems, temperate regions may be featured,
261 which are largely governed by delayed coupling. However, based on the lagging distribution limb
262 these delays could be further classified into (i) *dry-delay*, and (ii) *wet-delay*. The regions where
263 surface SM drying (or wetting) does not produce quicker imprints on ET, fall under the purview
264 of dry (or wet) delayed systems. These can be inferred from spatial maps of fraction of time a pixel
265 spends in dry or wet regime at any given season. The advantage of such a division is that it naturally
266 advances the widely accepted ideas of preferential states of soil moisture (D'Odorico & Porporato,
267 2004; Grayson et al., 1997; Sehgal & Mohanty, 2023) and Budyko framework (Budyko, 1974),
268 while forgoing earlier terminology conflicts. Additionally, the division allows for quantification
269 of SM-ET coupling using d_w which has extensions to understand corresponding entropy
270 production (described in section 3.4) in SM to ET anomaly transference. It is to be noted that the
271 proposed division leverages on the fact that vertical forces are dominant over lateral forces and
272 gravity drainage is seldom captured at footprint scale (Sehgal et al., 2021), hence, all SM anomalies

273 retrieved are registered as ET anomalies. This simplification provides flexibility in application of
 274 mass continuity equation (and thus *pdf* conservation).



275

276 **Figure 1.** Schematic describing the proposed SM-ET coupling from (a) hydro-mechanical

277 perspective to corresponding (b) statistical physics perspective condensed in the form of SM (blue)

278 and ET (green) anomaly impact factor (AIF) distributions. Grey arrow from a single SM_{AIF} (blue

279 circle) to most likely ET_{AIF} (green circle) represents transport instance satisfying optimal cost

280 function. Wasserstein distance (d_w) is the mean value of the square of optimal transportation

281 distance represented by the length of the arrows connecting all perturbation points from SM_{AIF} to

282 ET_{AIF} . (c) Based on Anomaly Impact Factor (AIF) values, global SM-ET coupling schemes are

283 divided broadly into dry coupled ($AIF < 0$) and wet-coupled ($AIF > 0$) systems. These can be

284 further divided into immediate coupling represented by closely spaced AIF distributions with

285 $d_w < 1$, and delayed coupling represented by distanced AIF distributions with high $d_w > 1$.

286

287 **3.4 Lower bound of Entropy production and Wasserstein Distance relationship**

288 Due to the open-system attributes of the land surface, both heat and mass flow across its
 289 boundaries producing entropy, with the transport of latent heat by vapor flux being the significant
 290 coupling process (Ouedraogo et al., 2013). Benamou & Brenier (2000) were able to prove that for
 291 a particle obeying diffusion equation of the form expressed in equation 3, the d_W bears direct
 292 linkage to continuum mechanics formulation that states: (1) d_W gives the lower bound on the
 293 expected value of the square of the effective velocity field $v_{eff}(x)$,

$$294 \quad d_W^2 \leq \tau \int_0^\tau \int ||v_{eff}(x)||^2 p_t(x) dx dt \quad (9)$$

295 where $p_t(x)$ is the probability density of the particle's position at any time t , and (2) the local mean
 296 velocity can be related to entropy production as

$$297 \quad \Sigma_t = \frac{1}{\mu T} \int ||v_{eff}(x)||^2 p_t(x) dx \quad (10)$$

298 where we consider the time integral from time $t = 0$ to time $t = \tau$. Comparing equations (9) and
 299 (10), the minimum entropy production associated with changing the probability density from an
 300 initial state s (in SM) to a final state e (in ET) can be expressed in terms of d_W ,

$$301 \quad \Sigma_t \geq \frac{1}{\mu T_{surf} \tau} d_W(s, e)^2 \quad (11)$$

302 where τ (s) is the duration of the anomaly transfer process or memory timescale, μ (s kg^{-1}) is water
 303 particle mobility, T_{surf} (K) is temperature of the land (soil + vegetation) surface, and Σ_t ($\text{J m}^{-2} \text{K}^{-1}$)
 304 is the entropy produced. Hence, for a stochastic process connecting the initial and final states,
 305 the right-hand side of equation 11 gives the lower bound on the entropy production, say Σ^* . An
 306 important consequence of equation 11 is the existence of a unique thermodynamic force which
 307 realizes minimal dissipation (Dechant & Sakurai, 2019).

308 Kinetic theory of gases defines mobility (μ) of a particle as the ratio of drift velocity and
 309 force field. From an analogous treatment, we consider the directional movement of water
 310 molecules as the “effective” velocity with which they are transported in the SVA continuum under
 311 an applied force field. So, the water particle mobility can be written as:

$$312 \quad \mu = \frac{v_{eff}}{F_{eff}} \quad (12)$$

313 From Newton’s second law:

$$314 \quad F_{eff} = \frac{d(mv_{eff})}{dt} = m \times \left(\frac{dv_{eff}}{dt} \right) + v_{eff} \times \left(\frac{dm}{dt} \right) \quad (13)$$

315 The rate of change in effective velocity (*first term*) is order of magnitudes smaller than mass flux
 316 contribution (*second term*), and hence can be neglected, giving a first order approximation of
 317 equation (13):

$$318 \quad F_{eff} \equiv v_{eff} \times \left(\frac{dm}{dt} \right) \quad (14)$$

319 This mass flux on a footprint scale is the amount of water vapor leaving the surface, i.e., physically
 320 equivalent to ET (kg s^{-1}),

$$321 \quad F_{eff} \equiv v_{eff} \times \text{ET} \quad (15)$$

322 From equation (12) and (15) we obtain

$$323 \quad \mu = \frac{1}{\text{ET}} \quad (16)$$

324 Here we note that the mass flux leaving the surface is dependent on external parameters
 325 such as temperature, vapor gradient, partitioning of net radiation, roughness of land surface, etc.
 326 but following the argument by (Brutsaert, 2014) that the moment-to-moment changes of these
 327 additional factors compensate each other, these are omitted for brevity. Hence, on a footprint scale,

328 this force and resulting field enables the effective water particle mobility which can be equivalently
 329 expressed as the inverse of ET expressed in kg s^{-1} (supplementary material),

$$330 \quad \Sigma^* = \frac{ET}{T_{surf} \tau} d_W(s, e)^2 \quad (17)$$

331 ***3.5 Optimization entanglement and the physical significance of Wasserstein Distance***

332 Using classical formulations, earlier literatures (Kleidon, 2008; Porada et al., 2011)
 333 proposed entropy production for ET to be function of chemical potential gradient ($\Delta\omega$) between
 334 atmospheric boundary layer and diffusing surface:

$$335 \quad \Sigma = \frac{ET}{T_{surf}} \Delta\omega \quad (18)$$

336 The diffusing surface, here, denotes the surface from where water particle escapes to the
 337 atmosphere, for example, soil surface for a barren open land or leaf surface for a vegetated area.
 338 The chemical potential of water is defined as the free energy per mole of water and elaborates the
 339 potential for a substance to move, or in other words, to do work. The statistical formulation (Eqn.
 340 17) and classical formulation (Eqn. 18) are analogues in construction. By introducing a constant
 341 of proportionality, we can equate both the formulations to obtain:

$$342 \quad d_W(s, e)^2 = \ell \cdot \tau \cdot \Delta\omega \quad (19)$$

343 where ℓ is proportionality constant (expressed in kg/J-s) which establishes a connection between
 344 the statistical and classical formulation. The product ($\tau \cdot \Delta\omega$) in eqn. (14) is equivalent to
 345 *action* (per unit mass) in classical mechanics which describes how a physical system evolves over
 346 time. Mathematically, action is a functional which takes the trajectory of the system as its argument
 347 and integrated over time span of state evolution. Hence, it is path dependent and the principle of
 348 least action (Sussman & Wisdom, 2001) postulates that the path followed by a physical system is
 349 that for which the action is minimized. In the context of SM-ET coupling, it means that the water

350 particle will always follow the path that minimizes the time-averaged $\Delta\omega$. Therefore, τ and $\Delta\omega$ are
 351 entangled such that the product $(\tau \cdot \Delta\omega)$ will always be optimized. As such, the optimization of
 352 d_W from MG minimization problem can be rooted in terms of classical treatment as the
 353 optimization (minimization) of entangled space of values for $(\tau \cdot \Delta\omega)$. Thus, d_W as the Euclidean
 354 length-scale can be defined as the path equivalent that optimizes $(\tau \cdot \Delta\omega)$ for a unit water potential
 355 gradient. In other words, optimization of SM-ET coupling leads to $(\tau \cdot \Delta\omega)$ entanglement giving
 356 the lower bound on the entropy production as the action measured by the path length of the d_W
 357 (Nakazato & Ito, 2021).

358 **3.6 Memory timescale formulation**

359 By virtue of this entanglement, the optimization formulation yields:

$$360 \quad \frac{\partial(\tau \cdot \Delta\omega)}{\partial d_W^2} = 0 \quad (20)$$

361 Expanding by chain rule, we obtain:

$$362 \quad \Delta\omega \times \frac{\partial(\tau)}{\partial d_W^2} + \tau \times \frac{\partial(\Delta\omega)}{\partial d_W^2} = 0 \quad (21)$$

$$363 \quad \Delta\omega \times \frac{\partial(\tau)}{\partial d_W^2} + \tau \times \frac{1}{\gamma} = 0 \quad (22)$$

364 where γ is the seasonal slope of d_W^2 versus $\Delta\omega$ plot and describes the sensitivity of SM-ET
 365 coupling to the induced potential gradients. Dividing (22) by $\Delta\omega$, we obtain:

$$366 \quad \frac{\partial(\tau)}{\partial d_W^2} + \frac{1}{\gamma\Delta\omega} \times \tau = 0 \quad (23)$$

367 Equation (23) represents a first order homogeneous differential equation whose solution is:

$$368 \quad \tau = \tau_0 \exp\left(\frac{-d_W^2}{\gamma\Delta\omega}\right) \quad (24)$$

369 where τ_0 is the integral constant, hereon defined as the inherent timescale of anomaly transference.
 370 The dimensionless quantity (τ/τ_0) can be used as a fundamental descriptor of water-energy
 371 coupling for a hydroclimate under induced potential gradients. To keep the problem tractable, we
 372 will consider a rudimentary approximation of $\tau_0 = L_d/K_{eff}$, where L_d is the traverse length for
 373 water particle, and K_{eff} is the effective conductivity of the land surface. We acknowledge that the
 374 solution for eqn. (24) is dependent on the initial value τ_0 whose approximation using rudimentary
 375 approach may not be appropriate for all cases but nevertheless, it provides a first order estimation
 376 of τ for testing our hypothesis and comparing it with results from earlier literatures.

377 **3.7 Chemical potential gradient as thermodynamic force**

378 To understand the functional form of the optimization entanglement, we compute chemical
 379 potential gradient ($\Delta\omega$) which is the absolute difference between atmospheric boundary layer
 380 potential and diffusing surface potential:

$$381 \quad \Delta\omega = |\omega_{bl} - \omega_{surf}| \quad (25)$$

382 where $\omega_{surf} = (\omega_{soil} + \omega_{veg})$ is the diffusing surface potential. The potential of water vapor in
 383 the atmospheric boundary layer is computed as:

$$384 \quad \omega_{bl} = R_{vap}T_{air}\ln(RH) + gz_{air} \quad (26)$$

385 where R_{vap} is the specific gas constant of water vapor ($= 461.5\text{J kg}^{-1} \text{K}^{-1}$), T_{air} and RH are the
 386 mean temperature and relative humidity of the boundary layer, respectively, g is the acceleration
 387 due to gravity, and z_{air} is the height of measurement relative to mean sea level. Pixels with $RH >$
 388 1 (*super saturated condition*) were removed from the analysis. The water potential in the
 389 vegetation is computed using:

$$390 \quad \omega_{veg} = (\theta_{veg} - 1.0) \times \Psi_{PWP} \quad (27)$$

391 θ_{veg} is the relative vegetation water content and Ψ_{PWP} is the permanent wilting point which is set
 392 to an upper threshold of 1471.5 J kg^{-1} (Porada et al., 2011). The vegetation water content (in kg m^{-2})
 393 was derived from normalized difference vegetation index (NDVI) data using SMAP algorithm
 394 (Chan, 2013):

$$395 \quad \theta^*_{veg} = (1.9134 \times NDVI^2 - 0.3215 \times NDVI) + stem\ factor \times \left(\frac{NDVI_{max} - NDVI_{min}}{1 - NDVI_{min}} \right) \quad (28)$$

396 The soil water potential is a sum of matric (Ψ_m) and gravitational (gz_{surf}) potential.

$$397 \quad \omega_{soil} = \Psi_m + gz_{surf} \quad (29)$$

398 where z_{surf} is the depth of water table from soil surface. Because we are concerned with the
 399 difference in potential $\Delta\omega$, the difference in gravitational potential ($z_{air} - z_{surf}$) g is taken an
 400 average value of $2 \times g$ as the values of reanalysis meteorological variables are quantified for a
 401 height of 2m above the land surface. For Ψ_m , we used van Genuchten (vG) soil water retention
 402 curve (SWC) (van Genuchten, 1980) for computation,

$$403 \quad S_{eff} = \frac{\theta - \theta_r}{\theta_s - \theta_r} = \frac{1}{[1 + (\alpha|\Psi_m|^n)]^{1-1/n}} \quad (30)$$

404 where $S_{eff}(-)$ is the effective saturation, θ ($\text{m}^3 \text{ m}^{-3}$) is the soil moisture reading, θ_s ($\text{m}^3 \text{ m}^{-3}$) is
 405 saturated water content, θ_r ($\text{m}^3 \text{ m}^{-3}$) is residual water content, α (m^{-1}) is inverse of the air entry
 406 pressure, n (-) is measure of the pore-size distribution, and Ψ (m) is the soil matric potential. Gupta
 407 et al. (2022 and 2020) provide maps of global vG parameters values (α , n , θ_r and θ_s) and saturated
 408 hydraulic conductivity (K_s) at field scale (i.e., 1 km spatial resolution). For converting these field-
 409 scale parameters to footprint scale effective values, we employ the upscaling guidelines set by Zhu
 410 & Mohanty (2002) for heterogeneous soils with variable saturation: arithmetic means for K_s and
 411 n , a value between arithmetic and geometric means for α when K_s and α are highly correlated, and
 412 a value between geometric and harmonic means for α when K_s and α are poorly correlated. Note

413 that correlation here refers to the parameter correlation of the coherency spectrum. For
 414 computation of τ_0 , L_d was approximated to canopy height + top soil depth (= 0.05m), while
 415 effective hydraulic conductivity was computed using series formulation, i.e., $K_{eff} =$
 416 $(K_{plant} \times K_{soil}) / (K_{plant} + K_{soil})$ for vegetated surface and $= K_{soil}$ for barren lands, expressed in
 417 m/s. Note that to reduce the artificial speckling effect introduced due to piecewise regression for
 418 computing γ , we smooth out the resulting raster for τ using a focal aggregation of 7x7 window.

419

420 **4. Results and Discussion**

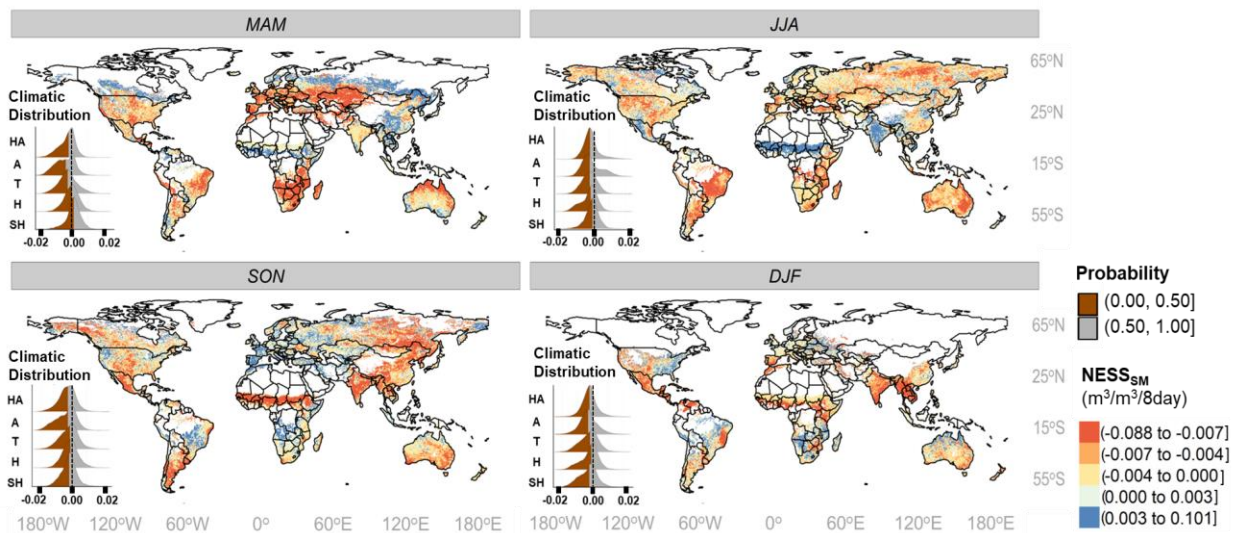
421 ***4.1 Global Non - Equilibrium Steady States of SM (NESS_{SM}) and ET (NESS_{ET})***

422 Fig. 2 and 3 showcase the seasonal variation in NESS_{SM} and NESS_{ET} globally. The non-
 423 equilibrium situation is caused by replacing the partially saturated air with relatively drier air
 424 parcels by continuous atmospheric circulation which results in a macroscopic thermodynamic non-
 425 equilibrium between SM and ET. Soil drying (negative NESS_{SM}) is dominantly prevalent across
 426 landscapes except when atmospheric forcings such as precipitation or melting of snow causes soil
 427 to predominantly wet. Whereas the spatial structuring for NESS_{ET} reflects seasonally dominant -
 428 latitudinal patterns with southward successive shifts in positive NESS_{ET}, starting from northern-
 429 mid latitudes in MAM, to northern-tropical latitudes in JJA and to southern counterparts during
 430 SON and DJF seasons.

431 During MAM, wet anomaly (positive NESS_{SM}) is prevalent at higher latitudes, Sahel
 432 region of Africa, eastern Asia (Central and Northeastern China, North Korea, Laos, Cambodia,
 433 Thailand, and Vietnam), and parts of southern Australia. During JJA, the monsoonal rainfall in
 434 Sahel region, Indian subcontinent and the western Mexico intensifies the wetting of soil (Fig. 2).
 435 The dual availability of moisture and energy allows the monsoonal imprints observed in NESS_{SM}

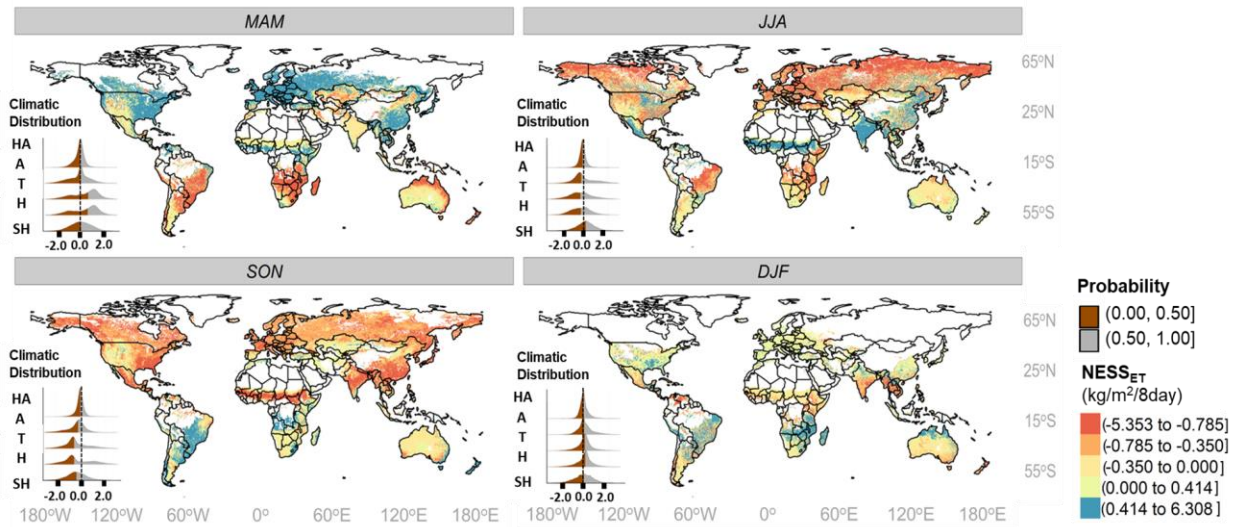
436 to be transferred to $NESS_{ET}$ with increasing flux rates throughout JJA (Fig 3). However, these
 437 regions undergo a complete reversal in the following seasons of SON and DJF.

438 Global arid and hyper-arid regions (western CONUS, Iberian Peninsula, central west
 439 Australia, southern Africa, and southern east South America) display a declining flux rate
 440 throughout all seasons. Interestingly, most of the CONUS spends more time drying soil than
 441 wetting except evergreen forest in northwestern coastline in SON (Fig. 2). One important attribute
 442 in case of Australian climate is the central deserted region which across all seasons remain in the
 443 desiccated state or nearly zero $NESS_{SM}$ which is a physical manifestation of low moisture leading
 444 to lower capacity to lose moisture further. The insets in Fig. 2 and 3 represent variations of $NESS_{SM}$
 445 and $NESS_{ET}$ observed across hydroclimates. These insets highlight two unique features about
 446 seasonal climatic distribution (i) compared to $NESS_{SM}$, a higher *in-class* variance is observed in
 447 $NESS_{ET}$, a characteristic most likely attributed to atmospheric fluctuations, and (ii) across classes,
 448 the seasonal variability is higher in temperate climates followed by humid regions, while super
 449 humid and hyper arid regions display relatively stable cross-season distribution.



450
 451 **Figure 2.** Global maps of Non-Equilibrium Steady State ($NESS_{SM}$) for four seasons - MAM, JJA,
 452 SON, and DJF. Insets show relative distribution of $NESS_{SM}$ amongst global hydroclimates (SH:

453 Super Humid, H: Humid, T: Temperate, A: Arid, HA: Hyper Arid). The vertical dashed line (black)
 454 in insets represent $NESS_{SM}$ of zero. The color sequential follows an approximate quantile division
 455 of data points. Missing/masked data are represented in white color.
 456



457
 458 **Figure 3.** Global maps of Non-Equilibrium Steady State ($NESS_{ET}$) for four seasons - MAM, JJA,
 459 SON, and DJF. Insets show relative distribution of $NESS_{ET}$ amongst global hydroclimates (SH:
 460 Super Humid, H: Humid, T: Temperate, A: Arid, HA: Hyper Arid). The vertical dashed line (black)
 461 in insets represents $NESS_{ET}$ of zero. The color sequential follows an approximate quantile division
 462 of data points. Missing/masked data are represented in white color.
 463

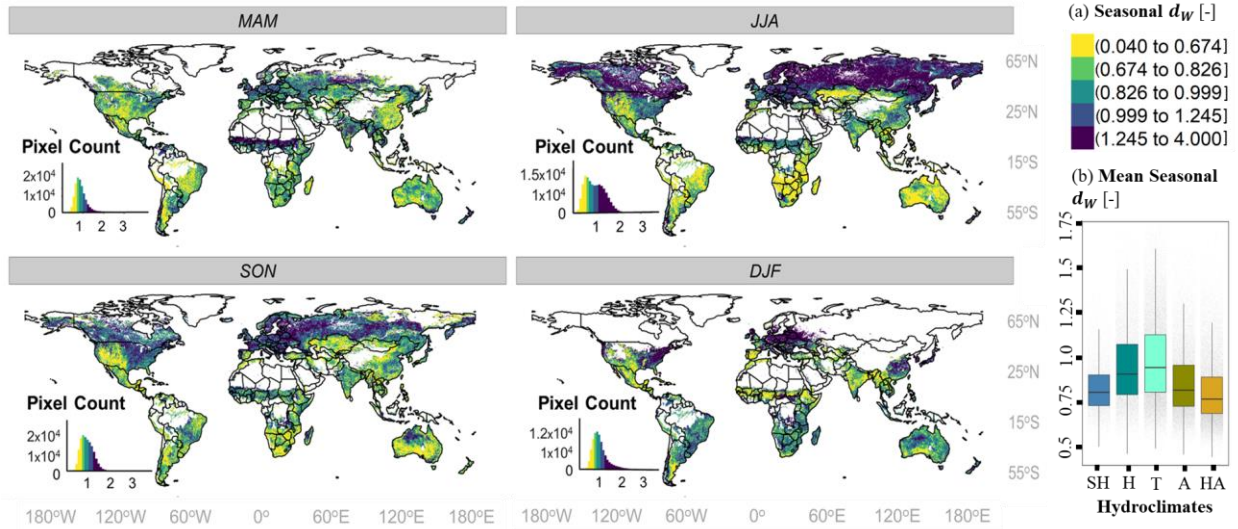
464 4.2 Global Wasserstein Distance (d_W) and the Coupling-Aridity Tradeoff

465 Fig. 4 showcases the seasonal variation in global d_W . A clear east-west division across
 466 CONUS is apparent in most seasons, however, the difference peaks during summer (JJA) and
 467 autumn (SON) months, albeit their causes remain divergent (explained through supplementary Fig.
 468 S1). Specifically, during JJA, eastern CONUS exhibits a fluctuating SM trailed by ET with land
 469 surfaces adjusting to the scattered patterns with the wet-delay enhancing as SON approaches.

470 Interestingly western CONUS exhibits lower d_W (i.e., immediate coupling) throughout summer
471 (JJA) and autumn (SON) but the coupling shifts from preferentially dry to wet (insets in Fig. S1a).
472 Similarly, the evergreen forests on the northwest corridor of CONUS showcase higher d_W which
473 could be attributed to the lower impact of surface moisture on ET, indicating the resilience to
474 hydrological droughts. A unique characteristic of continental climates such as Kazakhstan and
475 Mongolia were the oscillating behavior between dry-coupled state in JJA to wet-coupled state in
476 SON (insets in Fig. S1b). Such a strong oscillation could be attributed to the effect of hot winds
477 from Iranian deserts during summer and the effect of cold air front from polar regions in winter,
478 conjoined with meager oceanic influence. The insets provide histograms with wider variance in
479 JJA as larger numbers of pixel values are available/retrieved. Interestingly, regions located at
480 higher latitudes of North America, Europe and Asia displayed high d_W in JJA, however, we found
481 a latitudinal partitioning (insets in Fig. S1a) existing between mid-northern latitudes (undergoing
482 dry delay) and the northernmost corridor (undergoing a wet delay) preferably due to energy limited
483 state.

484 The spatial heterogeneity witnessed across seasons was captured in coupling-aridity
485 tradeoff (Fig. 4b) with temperate climates generally showing higher mean d_W (1.11 ± 0.25) while
486 the coupling metric tapers out on either extreme (0.83 ± 0.15 for SH and 0.81 ± 0.18 for HA)
487 (supplementary Table S3). This tradeoff bears implications on areas projected to witness stochastic
488 changes in precipitation, and thereby, on atmospheric and soil aridity (Maestre et al., 2016). For
489 instance, an increase in aridity would drag the SVA system into dry coupling state (lower d_W)
490 making it vulnerable to atmospheric dryness (such as heat dome formation during sustained heat
491 waves). Under such circumstances, surface moisture becomes crucial in guiding SM-ET coupling
492 and frequent soil desiccation will significantly impact the microbial and organic load of topsoil

493 (Berdugo et al., 2020). Besides coupling, however, the resilience of SVA systems needs
 494 accounting for the absolute capacity of anomaly transference which necessitates changes in
 495 system's entropy production.



496
 497 **Figure 4.** (a) Global maps of Wasserstein distance (d_W) signifying SM-ET coupling strength for
 498 four seasons - MAM, JJA, SON, and DJF. Insets show seasonal histogram of d_W . The color
 499 sequential follows a quantile division of data points. Missing/masked data are represented in white
 500 color. (b) Boxplots represent the global average distribution of d_W across hydroclimates (SH:
 501 Super Humid, H: Humid, T: Temperate, A: Arid, HA: Hyper Arid).

502

503 *4.3 Complimentary evolution pathways for climatic regimes*

504 During evolution, diverse paths of energy dispersal are explored in search of optimality
 505 (Feynman, 1948). This constrains the particles into obeying the entanglement ($\tau \cdot \Delta\omega$) obtained
 506 from principle of least action that couples the flow of energy with time. The memory timescale τ
 507 is, hence, a natural outcome of entanglement with energy flowing down the potential gradient
 508 between the potential ω_{bl} at the atmospheric boundary layer and ω_{surf} at the land surface. These

509 flows of energy propel systems towards more probable NESS eventually acquiring quasi-
 510 stationarity with respect to the surroundings (Tuisku et al., 2009).

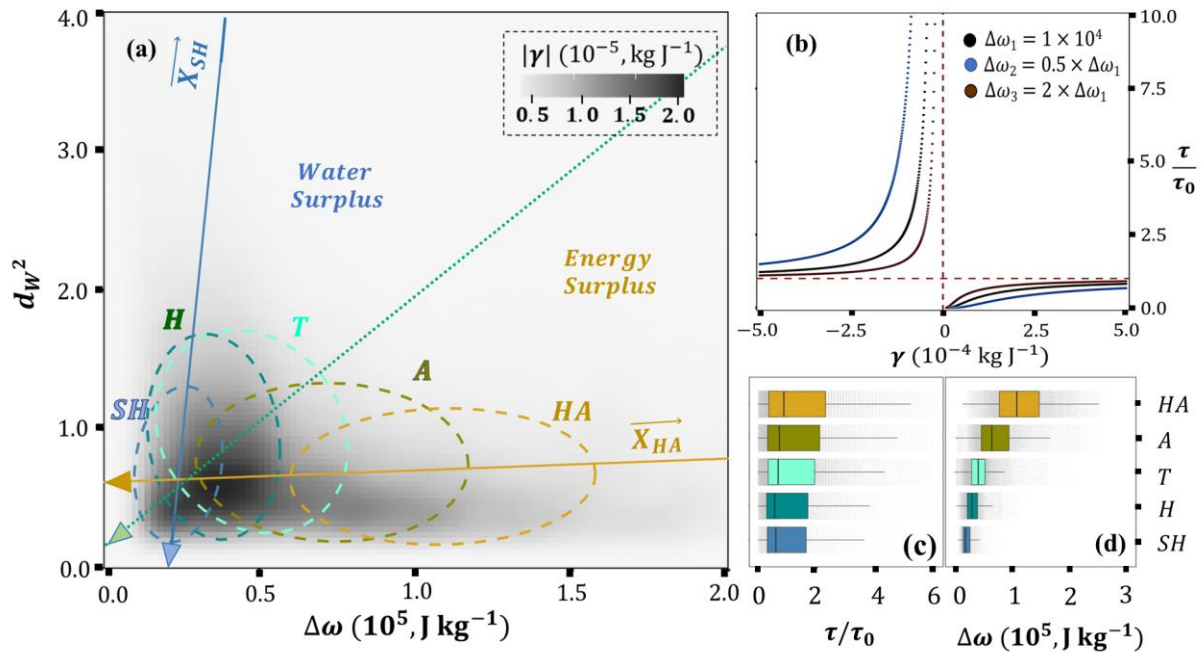
511 Figure 5a shows the joint density plot for d_W^2 vs. $\Delta\omega$ matrix. The color gradient in grey
 512 scale reflects higher absolute values of slope factor γ . The dashed ellipses encompass the
 513 interquartile range of values for all the hydroclimates. The orientation of the climatic ellipses
 514 provides information about the relationship between the shifting dominant modes of evolution with
 515 changing aridity. The Eigenvectors associated with the major axis of the ellipse correspond to the
 516 dominant modes of evolution and characterizes the behavior of the system's state trajectory when
 517 subjected to the dynamics governed by the d_W^2 vs. $\Delta\omega$ matrix. For instance, the eigen vectors ($\overrightarrow{X_{SH}}$
 518 & $\overrightarrow{X_{HA}}$) point towards the dominant direction of evolution for super humid (SH) and hyper arid
 519 (HA) climates. The arrows indicate the tendency of the systems to diminish the driving potential
 520 $\Delta\omega$. The approximate orthogonality between $\overrightarrow{X_{SH}}$ and $\overrightarrow{X_{HA}}$ suggests the complimentary
 521 evolutionary pathways adapted by either extremes for mitigating driving potential $\Delta\omega$. Physically,
 522 this symbolizes the scarcity of resources (water limitation in case of arid climates and energy
 523 limitation in case of humid climates) that generates this bias for the diverse pathway emergence as
 524 means of effective evolution. This is substantiated through the zoning of water surplus versus
 525 energy surplus systems (Fig. 5a) delineated by the minor axis of temperate ellipse extended
 526 throughout the space.

527 As evident from Fig. 5a, the system's state converges towards the global maxima for $|\gamma|$
 528 over time, where γ value presents the sensitivity of SM-ET coupling to the driving force field. The
 529 convergence for all hydroclimates around this global maximum implicitly indicates the existence
 530 of optimal combination of coupling metric (d_W^2) and driving force ($\Delta\omega$). The influence of
 531 different directions of the state-evolution is also suggestive of the fact that the cost paid by the

532 hydroclimates in terms of memory timescale τ will be different. The global seasonal maps of
533 relative time (τ/τ_0) is provided in the supplementary Fig. S4. Although there is significant
534 heterogeneity in global values of (τ/τ_0), coherent regional patterns are also discernible. For
535 instance, in United States with the advent of fall (SON) and winter (DJF) seasons, the atmospheric
536 demand drops increasing τ/τ_0 for arid climates. Similarly, an increase in $\Delta\omega$ during spring (MAM)
537 and summer months (JJA) reduces τ/τ_0 value in the higher latitudes. Furthermore, Fig. S2 and S3
538 represent inversely correlated spatial distributions in regions with negative γ and vice-versa.

539 Figure 5b substantiates the global maxima existence through the theoretical sensitivity
540 plots for the relative time (τ/τ_0) as a function γ and $\Delta\omega$ for a unit d_W^2 . τ/τ_0 indicates the deviation
541 of actual memory timescale (τ) from inherent timescale (τ_0) of a pixel due to external driving
542 forces. An increase in absolute value of γ leads to stable values for relative time ($\tau/\tau_0 \rightarrow 1$), while
543 a decreasing absolute value of γ leads to unstable values for relative time ($\tau/\tau_0 \rightarrow 0$ or ∞). A
544 change in $\Delta\omega$ results in scaling of the τ/τ_0 without distorting the functional form. Figure 5c & 5d
545 verifies this with variation seen in global hydroclimates for τ/τ_0 due to changes in $\Delta\omega$, i.e., the
546 higher fluctuations of $\Delta\omega$ observed in arid climates creates extended diversions for the τ/τ_0 , and
547 the trend declines with increasing humidity.

548



549

550 **Figure 5. (a)** The optimum zone of confluence (global maximum) for hydroclimates (SH: Super

551 Humid, H: Humid, T: Temperate, A: Arid, HA: Hyper Arid) for d_w^2 vs. $\Delta\omega$ joint density plot with

552 major Eigenvectors (\vec{X}_{SH} & \vec{X}_{HA}) indicating differences in evolutionary pathways for superhumid

553 (SH) and hyper arid (HA) climates. Dashed ellipses represent inter-quartile domain occupied by

554 respective hydroclimates, while the inclined dotted line represents minor axis of temperate climate

555 ellipse, corresponding to zoning of energy limited and water limited systems. The arrows on the

556 eigen vectors indicate the tendency of systems to diminish the potential gradient to attain quasi-

557 stationarity. **(b)** Sensitivity of τ/τ_0 to change in slope factor γ and potential gradient $\Delta\omega$ for a

558 given coupling bound ($d_w^2 = 1.0$). **(c & d)** Hydroclimate wise boxplots for relative time (τ/τ_0)

559 and potential gradient $\Delta\omega$. The observed variations in $\Delta\omega$ is reciprocated through variations in

560 computed τ/τ_0 .

561

562 **4.4 Memory timescale and time-gradient entanglement**

563 Typically, literatures suggest that the time taken by landscapes to dissipate an anomaly
 564 may range from $\sim 10^3$ secs (molecular diffusion scale) to $\sim 10^7$ secs (seasonal scale) (Ghannam et
 565 al., 2016; Haghghi et al., 2013; Wang et al., 2004; Wu & Dickinson, 2004). This spectrum in
 566 memory timescale spanning across 4 orders of magnitude is suggestive of the diverse mechanisms
 567 at interplay in SM-ET coupling. The global map of median τ (denoted as $\hat{\tau}$) across all seasons
 568 (MAM, JJA, SON, DJF) and its pdf is shown in Figure 6a (i) and (ii), while its seasonal map is
 569 provided in suppl. Fig. S4. The general observation in spatial median structure reflects a declining
 570 value of $\hat{\tau}$ with an increase in landscape aridity. This can be profoundly observed for arid and
 571 hyperarid regions across all major continents which stems from higher atmospheric demand,
 572 leading to quicker moisture depletion compared to temperate and humid climates. Interestingly,
 573 the pdf structure is positively skewed with dashed vertical lines representing 2 days (1st quantile),
 574 9 days (median) and 30 (3rd quantile) days respectively. These values are in line with findings in
 575 earlier literatures that have reported timescales of 10.4 days for agricultural regions, < 20 days for
 576 grassland and > 30 days for regions with appreciable tree cover (Dardanelli et al., 2004; Teuling
 577 et al., 2006; McColl et al., 2017). The horizontal lines with arrows in Fig. 6a(ii) showcase the IQR
 578 spread of $\hat{\tau}$ observed for different hydroclimates, with a general trend of longer moisture
 579 dissipation timescale with increasing humidity.

580 Figure 6b showcases that the best fit for entanglement ($\tau \cdot \Delta\omega$) optimization takes the
 581 functional form of exponential decay, parameterized using limit factor (α) and decay constant (λ).
 582 Two corollaries follow from this:

- 583 a) The rate of change $d\tau/d\Delta\omega$ is proportional to its current value τ , i.e., $d\tau/d\Delta\omega = -\lambda\tau$.
 584 Hence, the decay constant (λ) signifies the susceptibility of a system to change its response
 585 time (τ) for a unit shift in potential gradient.

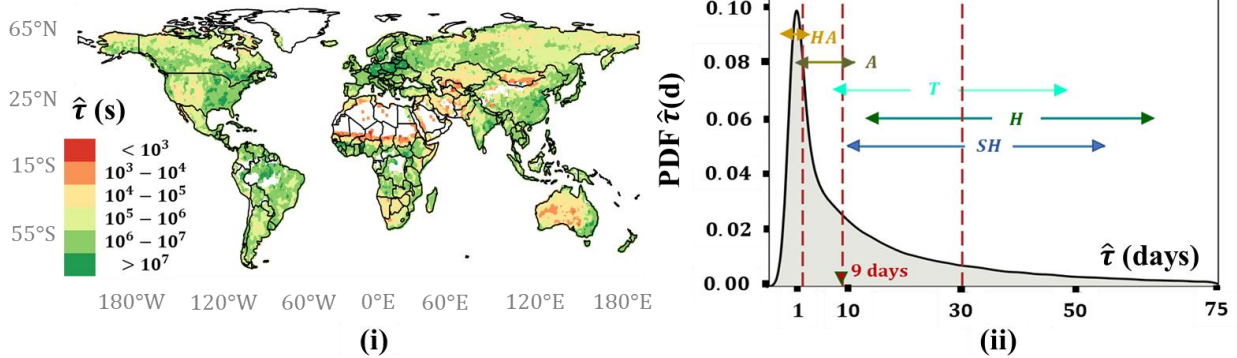
586 b) When the potential gradient diminishes to zero, i.e., $\Delta\omega \rightarrow 0$, the anomaly timescale will
587 tend to the limit factor, i.e., $\tau \rightarrow \alpha$.

588 The inset table in Fig. 6b provides median values for the α and λ for different hydroclimates
589 and the ensemble (all hydroclimates taken together). Global estimates of these parameters can be
590 crucial for predicting memory timescales for projected potential gradients in climate models
591 (Koster & Suarez, 2001). The ensemble fit gives a good efficiency of Kling-Gupta Efficiency
592 (KGE) of 0.54 with a decay rate of $1.10 \times 10^{-5} \text{ Kg J}^{-1}$ which is close to the temperate (T) climate
593 with reasonably good efficiency (KGE = 0.47). However, on either extreme on aridity scale, λ
594 value gets larger (with the exception for SH climate).

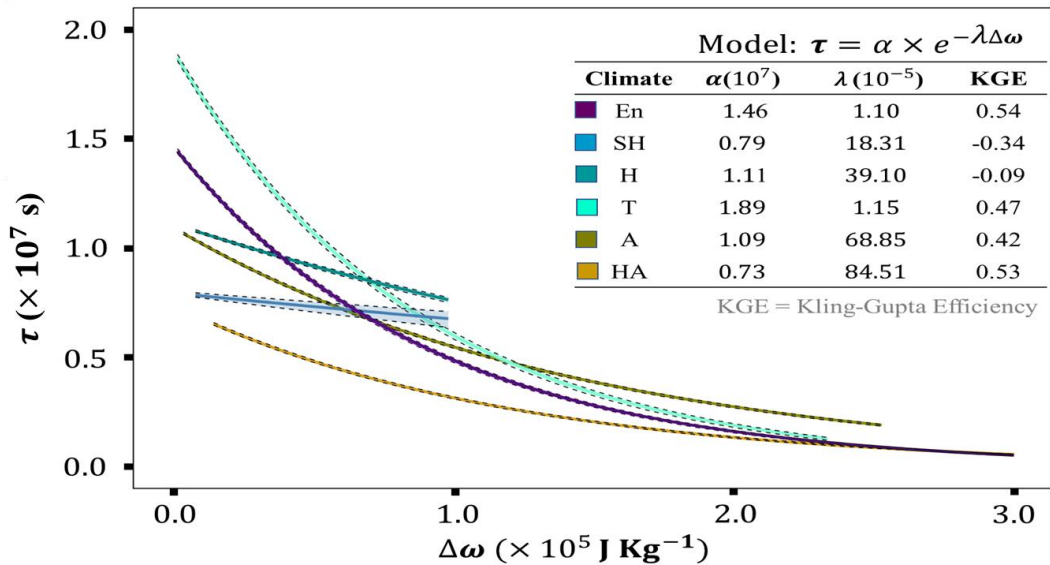
595 The faster decay of memory dissipation time for arid climates (Fig 6 (b)) can be ascribed
596 to concomitant turbulent diffusivity whereby, the vapor transport in the top soil ($\sim 2 - 4 \text{ cm}$) is
597 greatly enhanced by atmospheric turbulence (Brutsaert, 2014). This also suggests why a
598 deterministic loss model works for arid conditions (McColl et al., 2019). On the other hand, larger
599 λ values for humid climates can be attributed to the tendency of vegetation to lower their
600 conductivity in order to evade cavitation (Katul et al., 2012; Manzoni et al., 2013). The
601 incongruous behavior of SH model fit (KGE = - 0.34) is most likely due to significant
602 observational uncertainties from SM and ET remote sensing and meteorological reanalysis data.
603 Furthermore, the exponential decay model also implies the reasoning behind the emergence of
604 coupling-aridity tradeoff, with the optimized product ($\tau \cdot \Delta\omega$) value higher for temperate climates
605 relative to other climates. The non-linearity in time scale decay also signifies why usage of a linear
606 correlation coefficient or variations thereof by prior studies (Koster et al., 2004; Seneviratne et al.,
607 2010; Tuttle & Salvucci, 2016) might be a useful tool but can give contradictory results based on
608 the run time considered for the analysis.

609

(a) Seasonal Median



(b) Exponential Decay Model



610

611 **Figure 6. (a-i)** Global map of median memory timescale ($\hat{\tau}$) across all seasons. **(a-ii)** Probability

612 Density Function (pdf) of spatial distribution $\hat{\tau}$ values. The brown vertical dashed lines indicated

613 1st quartile, median, and 3rd quartile while horizontal bars show the IQR for different

614 hydroclimates. **(b)** Memory timescale as a function of potential gradient follows an exponential

615 decay model. Inset table quantifies the median values for fitted model parameters: α (limit factor)

616 and λ (decay constant). **4.5 Lower Bound of Entropy Production and its seasonal variations**

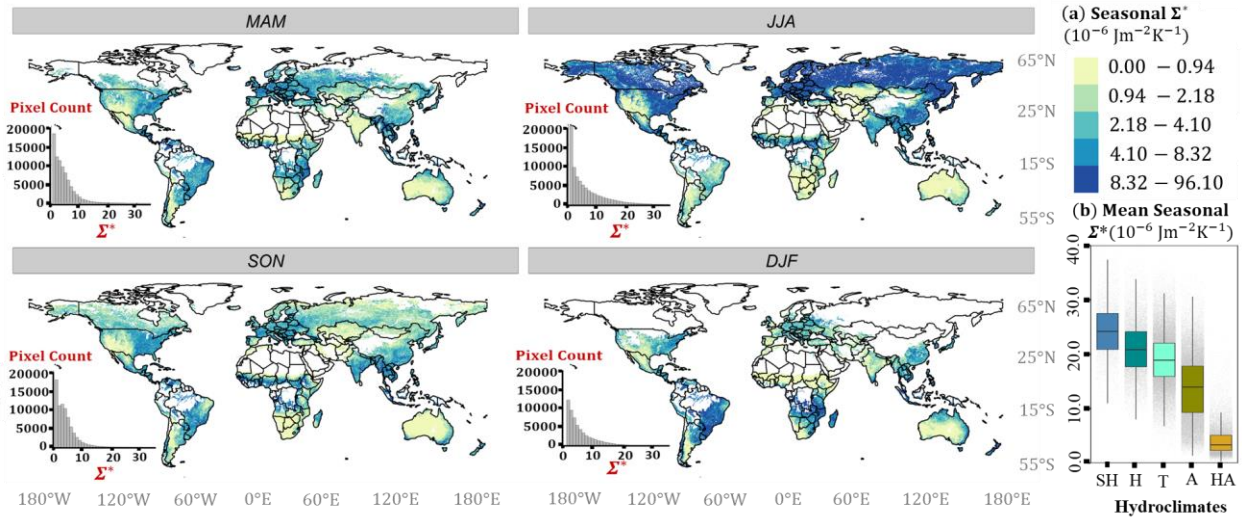
617 Although the concept of thermodynamics and entropy was first extensively introduced

618 back in 1943 (Edlefsen & Anderson, 1943), the theoretical understanding of how entropy

619 production is related to SM-ET coupling has been lacking. In practice, entropy production
620 manifests itself in the form of dissipation (Kleidon, 2022) of energy that is irreversibly lost into
621 the environment and hence, provides a quantitative characterization for investigating non-
622 equilibrium processes. For seasonal Σ^* computation, we consider the entire tri-month period, i.e.,
623 $\tau = 90$ days. Figure 7 shows that Σ^* varies greatly among regions, with predominant seasonal
624 patterns in tandem with ET variability. Throughout all seasons, global arid and hyperarid regions
625 produce lower amounts of entropy compared to vegetated and forested regions - primarily due to
626 lower SM availability. This transcends to higher fluctuations prevalent in most parts of Europe,
627 Russia, India, parts of Africa, and the northern borderline of Australia which mostly attribute to
628 humid or temperate regions with stronger climatic influences. Both availability of moisture and
629 energy drive entropy production, signifying the departure of the system from equilibrium
630 conditions - $NESS_{SM}$ and $NESS_{ET}$ away from zero. Wet soil surfaces enhance the total heat flux
631 from the surface into the boundary layer (Eltahir, 1998), thus producing higher entropy. Boxplots
632 (Fig. 7b) suggest higher entropy production in super humid ($24.30 \pm 5.25 \times 10^{-6} \text{ J m}^{-2} \text{ K}^{-1}$) and
633 humid ($21.10 \pm 4.88 \times 10^{-6} \text{ J m}^{-2} \text{ K}^{-1}$) regions and consistent decline in entropy with increase in
634 aridity (suppl. Table S4). These findings are similar to a previous simulation study (Kleidon, 2008)
635 which showcased that higher entropy is produced in regions with higher ET. However, the
636 inclusion of d_W in our study differentiates systems based on their ability in utilization of available
637 energy for unit anomaly transference. Thus, d_W can also be interpreted as an efficiency factor.
638 This is critical to understand how the variability in SM-ET coupling will affect the ability of
639 ecosystems to produce entropy which is a direct indicator of the capacity of the system to work.

640 Discrepancies in d_W hint to the fact that although entropy production is always positive,
641 different ways of performing the same operation may incur more or less dissipation (Dechant &

642 Sakurai, 2019). Another conjecture from the coupling-aridity tradeoff and entropy production
 643 capacity is that for a given amount of flux and land temperature, temperate climates bear the least
 644 efficiency compared to other hydroclimates for unit anomaly transference. This could be argued
 645 to be most likely due to their bistable nature for soil moisture subsidence (Sehgal & Mohanty,
 646 2023).



647 **Figure 7.** (a) Global maps of Entropy production (lower bound, Σ^*) for four seasons - MAM, JJA,
 648 SON, and DJF. Insets show seasonal histogram of Σ^* . The color sequential follows a quantile
 649 division of data points. Missing/masked data are represented in white color. (b) Boxplots represent
 650 the global average distribution of d_W across hydroclimates (SH: Super Humid, H: Humid, T:
 651 Temperate, A: Arid, HA: Hyper Arid).

653

654 *4.6 Dissipative Energy Barriers for Terrestrial Ecosystems*

655 Terrestrial biota substantially affects the exchange of fluxes rendering forests to be
 656 biologically the most productive ecosystem (Holdaway et al., 2010). However, maintenance of
 657 this productivity requires a continuous influx of solar energy and precipitation. Horowitz et al.,
 658 (2017) argue that to maintain an arbitrary non-equilibrium state, a minimum rate of energy must

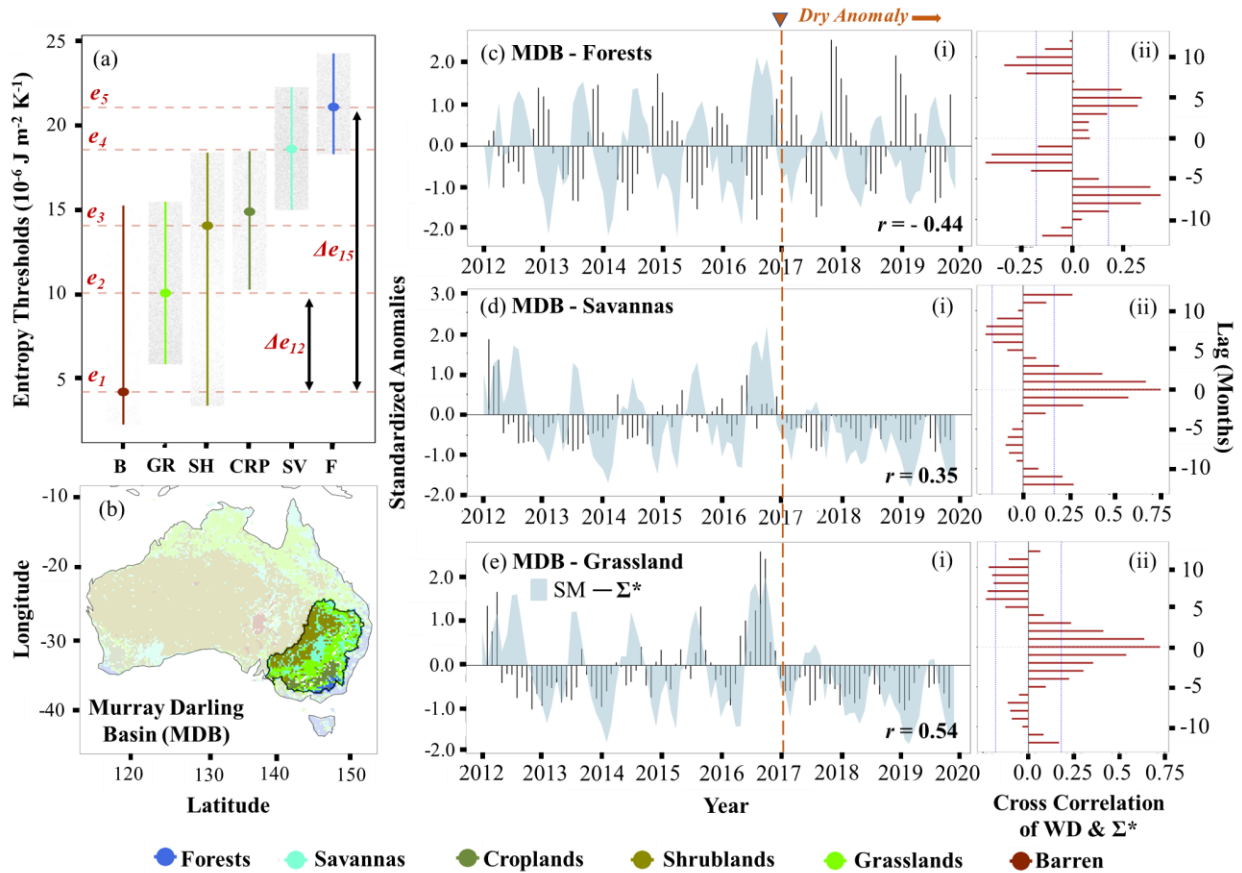
659 be supplied and dissipated by the system. Hence, the influx of energy to ecosystems is
660 accompanied by higher entropy production (or higher dissipation), implying a one-to-one
661 correspondence between productivity and dissipative energy state the system is in. Therefore, there
662 exists energetic barriers amongst ecosystems and by quantifying the amount of entropy production
663 from SM-ET coupling, we can place terrestrial ecosystems in the context of dissipative energy
664 states. Fig. 8a showcases global entropy thresholds for terrestrial ecosystems. Broadly, ecosystems
665 display a hierarchy of entropy thresholds (i.e., e_1 through e_5) with increasing median energy
666 dissipation levels from barren to forested ecosystems. Croplands are highly regularized systems
667 and hence are considered as a reference case with respect to other systems which are subject to
668 less human intervention. The difference in median energy levels represent the dissipative energy
669 barriers (Δe) between ecosystems. The quantitative values are provided in supplementary Tables
670 S5 and S6, while emphasis is laid on qualitative understanding in subsequent explanations.

671 One of the major imprints of climate change is projected to be global aridity shifts
672 concurrently affecting multiple ecosystem functioning (Berdugo et al., 2020; Huang et al., 2016;
673 Maestre et al., 2016). Earlier literatures have argued tropical forests and savannas to represent
674 alternative stable states (Hirota et al., 2011), which align consecutively in the entropy hierarchy
675 separated by an energy barrier Δe_{45} . Similarly, the lower we transcend in energy levels, the higher
676 the dissipative energy barriers become between two ecosystems. For instance, the tipping of barren
677 land ecosystems (with dissipative energy e_1) into forest ecosystems (with dissipative energy e_5)
678 requires overcoming an energy barrier of Δe_{15} which is $\sim 3 \times \Delta e_{12}$ i.e., tipping of barren lands into
679 grasslands. The lowest level of barren lands in entropy hierarchy is because of sparse vegetation
680 cover ($< 10\%$ according to IGBP definition) and relatively infertile soil, while as the vegetation
681 cover increases the dissipative capacity of the system improves. We argue that these energy

682 barriers prevent ecosystems from undergoing catastrophic shifts (van Nes et al., 2016; Scheffer et
683 al., 2001).

684 From the perspective of resilience, the ecosystem's response to perturbations could be
685 understood as the entropy produced in adjusting to atmospheric conditions. Ecosystems with
686 higher resilience will maintain their long-term seasonal behavior and gradually adapt or mitigate
687 the effects of stochastic anomalies. We illustrate this by considering the Murray - Darling basin
688 (MDB) in Australia for its diverse climate ranging from temperate in the south, subtropical in the
689 north, to semi-arid in the west, and entails a variety of ecosystems (Fig. 8b). MDB has experienced
690 a decline in rainfall, with area-average rainfall being lowest in the three years from Jan 2017 to
691 Dec 2019 (Australian Bureau of Meteorology, 2020). Our results indicate that the resilience
692 displayed to this dry period development, however, was different for different ecosystems (Fig. 8
693 c - e). Highest resilience was witnessed in forested ecosystems where changes in SM and Σ^* are
694 asynchronous (Pearson $r = -0.44$) with Σ^* often lagging SM (Fig. 8c (i)). Furthermore, an
695 insignificant cross-correlation factor (CCF) between d_W and Σ^* at 0 months lag (Fig. 8c (ii))
696 represents deviation of SM-ET coupling effect on Σ^* . On the contrary, for ecosystems with lower
697 dissipative energy levels (i.e., Savannas and Grasslands), we observe an increasing synchrony
698 (Pearson $r = 0.35, 0.54$) between SM and Σ^* (Fig. 8d-e (i)), most likely facilitated by increasing
699 effect of surface SM-ET coupling (significant CCF at 0 months lag) on Σ^* (Fig. 8d-e (ii)). This is
700 evident from a sustained negative SM and Σ^* anomaly throughout the dry period post 2017. In
701 other words, such systems are vulnerable to climate anomalies and respond quickly (lower
702 resilience). Hence, the results reflect upon two critical aspects (1) the variations in coping
703 dynamics of systems subjected to prolonged state of perturbations are governed by dissipative
704 energy levels at which the system can work, and (2) the tipping of a system will only be realized

705 when the corresponding energy barriers are crossed frequently enough when supported by changes
 706 in aridity and energy influx.



707
 708 **Figure 8.** (a) Global entropic thresholds for different ecosystems (B: Barren, GR: Grassland, SH:
 709 Shrubland, CRP: Cropland, SV: Savanna, F: Forest). The length of vertical bars represents IQR
 710 and points represent the median Σ^* values. The horizontal lines (red, dashed) represent the median
 711 entropy values or dissipative energy levels (e_1, e_2, e_3, e_4, e_5), and the difference represents
 712 corresponding dissipative energy barriers (Δe). (b) Study area of Murray Darling Basin (MDB) in
 713 Australia. (c-e) (i) Time series plots of standardized anomalies of soil moisture (blue) and entropy
 714 production (black); the dashed line (orange) demarcates beginning of dry period in MDB, and (ii)
 715 Cross-correlation between mean monthly d_W and Σ^* computed for a lag of 12 months; the vertical
 716 blue lines represent 95% confidence interval.

717

718 **5. Summary and Conclusion**

719 This study provides a global assessment of entropic thresholds across various
 720 hydroclimates and their relationship with ecosystem resilience. Existence of water potential
 721 gradient ($\Delta\omega$) is utilized to formulate and define non-equilibrium steady states (NESS) as the state
 722 with nonzero fluxes and nonzero potential gradients (Qian, 2006) that hydroclimates hold-on to by
 723 dissipating energy to the environment. This dissipation physically manifests as entropy production
 724 when an imposed soil moisture (SM) anomaly is transferred to evapotranspiration (ET). For
 725 quantifying this SM-ET coupling and its relationship with entropy production, we introduce a new
 726 metric called the *Wasserstein distance* (d_W). The metric d_W is typically used in optimal transport
 727 (OT) discipline, and provides a measure of time evolution of probability density of a diffusing
 728 particle from one state to the other. Thus, d_W gives a new paradigm in deciphering system
 729 evolution through SM-ET coupling as water particle transitions in SVA continuum from soil to
 730 atmosphere. The global seasonal analysis for SM-ET coupling using remote sensing surface SM
 731 and ET data, establishes a “*coupling-aridity tradeoff*” with temperate climates operating at lower
 732 efficiencies per unit of flux and given surface temperature. This tradeoff bears greater implications
 733 on areas projected to witness aridity shifts in the future.

734 The optimization of SM-ET coupling transcends to $(\tau \cdot \Delta\omega)$ entanglement, which is
 735 equivalent to *action* (per unit mass) in classical mechanics describing how a physical system
 736 evolves over time. Obeying *principle of least action* in the context of SM-ET coupling, ascertains
 737 that water particles follow the path that minimizes the time-averaged $\Delta\omega$. The memory timescale
 738 (τ) is, hence, a natural outcome of $(\tau \cdot \Delta\omega)$ entanglement with energy flowing downhill. We apply
 739 this principle globally to compute τ which spans across four orders of magnitude, i.e., from

740 molecular diffusion scale ($\sim 10^3$ s) to seasonal scale ($\sim 10^7$ s). The wider spectrum of timescales
 741 observed could be attributed to the scarcity of resources (water limitation versus energy limitation)
 742 that generates an evolutionary preference for hydroclimates. Through eigenvalue analysis, we
 743 prove the existence of such complementary evolution routes for major hydroclimates which are in
 744 search for an optimal combination of coupling metric (d_W) and driving potential ($\Delta\omega$). Such an
 745 optimum is possible when both physical and physiological controls on terrestrial water-energy
 746 coupling work on a “*similar strategy*” to mitigate atmospheric perturbations.

747 Extending the coupling formulation to compute lower bounds of entropy production (Σ^*),
 748 we observe that global arid and hyperarid regions produce less entropy compared to vegetated and
 749 forested regions - primarily due to lower SM availability. The major terrestrial ecosystems arrange
 750 themselves in a hierarchy of median entropic thresholds, with barren lands occupying the lowest
 751 level. The difference in these median entropic values represent the dissipative energy barriers
 752 (DEB) which prevents tipping of one ecosystem into another. The emergence of hierarchical DEB
 753 answers (1) why an inertia exists for systems to return to pre-anomaly conditions, and (2) if a
 754 tipping occurs, to which state the transition might happen! These findings are crucial for predicting
 755 how global ecosystems will respond to changing climate and for imposing effective constraints for
 756 simulating land-surface fluxes under a range of atmospheric forcings.

757

758 **6. Acknowledgements**

759 The authors acknowledge the funding support from NASA SMAP project
760 (80NSSC20K1807). We thank the Texas A&M High-Performance Research Computing (HPRC)
761 for providing computing resources for the research.

762

763 **7. Open Research**

764 C3S soil moisture is available at Copernicus climate data store (CCD):
765 <https://cds.climate.copernicus.eu/cdsapp#!/dataset/satellite-soil-moisture?tab=overview>. Terra
766 MODIS Net Evapotranspiration product (MOD16A2GF) is available at NASA LPDAAC:
767 <https://lpdaac.usgs.gov/products/mod16a2gfv006/>. Bias-corrected near surface meteorological
768 data is available at: [https://cds.climate.copernicus.eu/cdsapp#!/dataset/derived-near-surface-](https://cds.climate.copernicus.eu/cdsapp#!/dataset/derived-near-surface-meteorological-variables?tab=overview)
769 [meteorological-variables?tab=overview](https://cds.climate.copernicus.eu/cdsapp#!/dataset/derived-near-surface-meteorological-variables?tab=overview). Soil physical properties can be downloaded from:
770 <https://files.isric.org/soilgrids/latest/>. Soil water characteristic parameters are available at:
771 <https://zenodo.org/record/6348799#.ZBn-y3bMKUn>. Terra MODIS GPP product (MOD17A2H)
772 is available at: <https://lpdaac.usgs.gov/products/mod17a2hv006/>, NDVI (MOD13A1) product is
773 available at: <https://lpdaac.usgs.gov/products/mod13a1v006/>, and LAI product (MOD15A2H) is
774 available at: <https://lpdaac.usgs.gov/products/mod15a2hv006/>. All MODIS data products were
775 downloaded using Application for Extracting and Exploring Analysis Ready Samples
776 (AppEEARS). Global estimates of coupling metric (d_w), entropy bounds (Σ^*) and memory
777 timescales (τ) can be found in supplemental material.

778

779 **References**

- 780 Annala, A., & Kuismanen, E. (2009). Natural hierarchy emerges from energy dispersal.
 781 *BioSystems*, 95(3), 227–233. <https://doi.org/10.1016/j.biosystems.2008.10.008>
- 782 Benamou, J.-D., & Brenier, Y. (2000). A computational fluid mechanics solution to the Monge-
 783 Kantorovich mass transfer problem. *Numerische Mathematik*, 84(3), 375–393.
 784 <https://doi.org/10.1007/s002110050002>
- 785 Berdugo, M., Delgado-Baquerizo, M., Soliveres, S., Hernández-Clemente, R., Zhao, Y., Gaitán,
 786 J. J., et al. (2020). Global ecosystem thresholds driven by aridity. *Science*, 367(6479),
 787 787–790. <https://doi.org/10.1126/science.aay5958>
- 788 Blöschl, G., & Sivapalan, M. (1995). Scale issues in hydrological modelling: A review. *Hydrological*
 789 *Processes*, 9(3–4), 251–290. <https://doi.org/10.1002/hyp.3360090305>
- 790 Brutsaert, W. (2014). Daily evaporation from drying soil: Universal parameterization with similarity.
 791 *Water Resources Research*, 50(4), 3206–3215. <https://doi.org/10.1002/2013WR014872>
- 792 Budyko, M. I. (1974). *Climate and life*. Academic press.
- 793 Crow, W. T., Berg, A. A., Cosh, M. H., Loew, A., Mohanty, B. P., Panciera, R., et al. (2012).
 794 Upscaling sparse ground-based soil moisture observations for the validation of coarse-
 795 resolution satellite soil moisture products. *Reviews of Geophysics*, 50(2).
 796 <https://doi.org/10.1029/2011RG000372>
- 797 Dardanelli, J. L., Ritchie, J. T., Calmon, M., Andriani, J. M., & Collino, D. J. (2004). An empirical
 798 model for root water uptake. *Field Crops Research*, 87(1), 59–71.
 799 <https://doi.org/10.1016/j.fcr.2003.09.008>
- 800 Dechant, A. (2022). Minimum entropy production, detailed balance and Wasserstein distance for
 801 continuous-time Markov processes. *Journal of Physics A: Mathematical and Theoretical*,
 802 55(9), 094001. <https://doi.org/10.1088/1751-8121/ac4ac0>
- 803 Dechant, A., & Sakurai, Y. (2019, December 18). Thermodynamic interpretation of Wasserstein
 804 distance. arXiv. <https://doi.org/10.48550/arXiv.1912.08405>

- 805 Dirmeyer, P. A. (2011). The terrestrial segment of soil moisture–climate coupling. *Geophysical*
806 *Research Letters*, 38(16). <https://doi.org/10.1029/2011GL048268>
- 807 D’Odorico, P., & Porporato, A. (2004). Preferential states in soil moisture and climate dynamics.
808 *Proceedings of the National Academy of Sciences*, 101(24), 8848–8851.
809 <https://doi.org/10.1073/pnas.0401428101>
- 810 Dong, J., Akbar, R., Short Gianotti, D. J., Feldman, A. F., Crow, W. T., & Entekhabi, D. (2022).
811 Can Surface Soil Moisture Information Identify Evapotranspiration Regime Transitions?
812 *Geophysical Research Letters*, 49(7), e2021GL097697.
813 <https://doi.org/10.1029/2021GL097697>
- 814 Dosio, A., Mentaschi, L., Fischer, E. M., & Wyser, K. (2018). Extreme heat waves under 1.5 °C
815 and 2 °C global warming. *Environmental Research Letters*, 13(5), 054006.
816 <https://doi.org/10.1088/1748-9326/aab827>
- 817 Edlefsen, N., & Anderson, A. (1943). Thermodynamics of soil moisture. *Hilgardia*, 15(2), 31–298.
- 818 Eltahir, E. A. B. (1998). A Soil Moisture–Rainfall Feedback Mechanism: 1. Theory and
819 observations. *Water Resources Research*, 34(4), 765–776.
820 <https://doi.org/10.1029/97WR03499>
- 821 Feldman, A. F., Short Gianotti, D. J., Trigo, I. F., Salvucci, G. D., & Entekhabi, D. (2022). Observed
822 Landscape Responsiveness to Climate Forcing. *Water Resources Research*, 58(1),
823 e2021WR030316. <https://doi.org/10.1029/2021WR030316>
- 824 Feynman, R. P. (1948). Space-Time Approach to Non-Relativistic Quantum Mechanics. *Reviews*
825 *of Modern Physics*, 20(2), 367–387. <https://doi.org/10.1103/RevModPhys.20.367>
- 826 Fu, Z., Ciais, P., Feldman, A. F., Gentine, P., Makowski, D., Prentice, I. C., et al. (2022). Critical
827 soil moisture thresholds of plant water stress in terrestrial ecosystems. *Science Advances*,
828 8(44), eabq7827. <https://doi.org/10.1126/sciadv.abq7827>

- 829 van Genuchten, M. Th. (1980). A Closed-form Equation for Predicting the Hydraulic Conductivity
830 of Unsaturated Soils. *Soil Science Society of America Journal*, 44(5), 892–898.
831 <https://doi.org/10.2136/sssaj1980.03615995004400050002x>
- 832 Ghannam, K., Nakai, T., Paschalis, A., Oishi, C. A., Kotani, A., Igarashi, Y., et al. (2016).
833 Persistence and memory timescales in root-zone soil moisture dynamics. *Water*
834 *Resources Research*, 52(2), 1427–1445. <https://doi.org/10.1002/2015WR017983>
- 835 Grayson, R. B., Western, A. W., Chiew, F. H. S., & Blöschl, G. (1997). Preferred states in spatial
836 soil moisture patterns: Local and nonlocal controls. *Water Resources Research*, 33(12),
837 2897–2908. <https://doi.org/10.1029/97WR02174>
- 838 Gupta, S., Hengl, T., Lehmann, P., Bonetti, S., Papritz, A., & Or, D. (2020). Global soil saturated
839 hydraulic conductivity map using random forest in a Covariate-based Geo Transfer
840 Functions (CoGTF) framework at 1 km resolution [Data set]. Zenodo.
841 <https://doi.org/10.5281/zenodo.3934854>
- 842 Gupta, S., Papritz, A., Lehmann, P., Hengl, T., Bonetti, S., & Or, D. (2022). Global maps of soil
843 water characteristics parameters developed using the random forest in a Covariate-based
844 GeoTransfer Functions (CoGTF) framework at 1 km resolution [Data set]. Zenodo.
845 <https://doi.org/10.5281/zenodo.6348799>
- 846 Haghghi, E., Shahraneeni, E., Lehmann, P., & Or, D. (2013). Evaporation rates across a
847 convective air boundary layer are dominated by diffusion. *Water Resources Research*,
848 49(3), 1602–1610. <https://doi.org/10.1002/wrcr.20166>
- 849 Hirota, M., Holmgren, M., Van Nes, E. H., & Scheffer, M. (2011). Global Resilience of Tropical
850 Forest and Savanna to Critical Transitions. *Science*, 334(6053), 232–235.
851 <https://doi.org/10.1126/science.1210657>
- 852 Holdaway, R. J., Sparrow, A. D., & Coomes, D. A. (2010). Trends in entropy production during
853 ecosystem development in the Amazon Basin. *Philosophical Transactions of the Royal*

- 854 *Society B: Biological Sciences*, 365(1545), 1437–1447.
 855 <https://doi.org/10.1098/rstb.2009.0298>
- 856 Horowitz, J. M., Zhou, K., & England, J. L. (2017). Minimum energetic cost to maintain a target
 857 nonequilibrium state. *Physical Review E*, 95(4–1), 042102.
 858 <https://doi.org/10.1103/PhysRevE.95.042102>
- 859 Huang, J., Yu, H., Guan, X., Wang, G., & Guo, R. (2016). Accelerated dryland expansion under
 860 climate change. *Nature Climate Change*, 6(2), 166–171.
 861 <https://doi.org/10.1038/nclimate2837>
- 862 Kaila, V. R. I., & Annala, A. (2008). Natural selection for least action. *Proceedings of the Royal
 863 Society A: Mathematical, Physical and Engineering Sciences*, 464(2099), 3055–3070.
 864 <https://doi.org/10.1098/rspa.2008.0178>
- 865 Katul, G. G., Oren, R., Manzoni, S., Higgins, C., & Parlange, M. B. (2012). Evapotranspiration: A
 866 process driving mass transport and energy exchange in the soil-plant-atmosphere-climate
 867 system. *Reviews of Geophysics*, 50(3). <https://doi.org/10.1029/2011RG000366>
- 868 Kleidon, A. (2010). A basic introduction to the thermodynamics of the Earth system far from
 869 equilibrium and maximum entropy production. *Philosophical Transactions of the Royal
 870 Society B: Biological Sciences*, 365(1545), 1303–1315.
 871 <https://doi.org/10.1098/rstb.2009.0310>
- 872 Kleidon, Axel. (2008). Entropy production by evapotranspiration and its geographic variation. *Soil
 873 and Water Research*, 3(Special Issue 1), S89–S94. <https://doi.org/10.17221/1192-SWR>
- 874 Kleidon, Axel. (2022). Working at the limit: A review of thermodynamics and optimality of the Earth
 875 system. *Earth System Dynamics Discussions*, 1–46. <https://doi.org/10.5194/esd-2022-38>
- 876 Koster, R. D., & Suarez, M. J. (2001). Soil Moisture Memory in Climate Models. *Journal of
 877 Hydrometeorology*, 2(6), 558–570. [https://doi.org/10.1175/1525-
 878 7541\(2001\)002<0558:SMMICM>2.0.CO;2](https://doi.org/10.1175/1525-7541(2001)002<0558:SMMICM>2.0.CO;2)

- 879 Koster, R. D., Dirmeyer, P. A., & Guo, Z. (2004). Regions of Strong Coupling Between Soil
880 Moisture and Precipitation. <https://doi.org/10.1126/science.1100217>
- 881 Lang, N., Jetz, W., Schindler, K., & Wegner, J. D. (2022, April 13). A high-resolution canopy height
882 model of the Earth. arXiv. <https://doi.org/10.48550/arXiv.2204.08322>
- 883 Lehmann, P., Assouline, S., & Or, D. (2008). Characteristic lengths affecting evaporative drying
884 of porous media. *Physical Review E*, 77(5), 056309.
885 <https://doi.org/10.1103/PhysRevE.77.056309>
- 886 Liu, Y., Holtzman, N. M., & Konings, A. G. (2021). Global ecosystem-scale plant hydraulic traits
887 retrieved using model–data fusion. *Hydrology and Earth System Sciences*, 25(5), 2399–
888 2417. <https://doi.org/10.5194/hess-25-2399-2021>
- 889 Lopez, A. (2018). Soil moisture gridded data from 1978 to present [Data set]. ECMWF.
890 <https://doi.org/10.24381/CDS.D7782F18>
- 891 Maestre, F. T., Eldridge, D. J., Soliveres, S., Kéfi, S., Delgado-Baquerizo, M., Bowker, M. A., et
892 al. (2016). Structure and Functioning of Dryland Ecosystems in a Changing World. *Annual*
893 *Review of Ecology, Evolution, and Systematics*, 47(1), 215–237.
894 <https://doi.org/10.1146/annurev-ecolsys-121415-032311>
- 895 Manzoni, S., Vico, G., Katul, G., Palmroth, S., Jackson, R. B., & Porporato, A. (2013). Hydraulic
896 limits on maximum plant transpiration and the emergence of the safety–efficiency trade-
897 off. *New Phytologist*, 198(1), 169–178. <https://doi.org/10.1111/nph.12126>
- 898 McColl, K. A., Wang, W., Peng, B., Akbar, R., Short Gianotti, D. J., Lu, H., et al. (2017). Global
899 characterization of surface soil moisture drydowns. *Geophysical Research Letters*, 44(8),
900 3682–3690. <https://doi.org/10.1002/2017GL072819>
- 901 McColl, K. A., He, Q., Lu, H., & Entekhabi, D. (2019). Short-Term and Long-Term Surface Soil
902 Moisture Memory Time Scales Are Spatially Anticorrelated at Global Scales. *Journal of*
903 *Hydrometeorology*, 20(6), 1165–1182. <https://doi.org/10.1175/JHM-D-18-0141.1>

- 904 McCurley Pisarello, K. L., & Jawitz, J. W. (2021). Coherence of global hydroclimate classification
905 systems. *Hydrology and Earth System Sciences*, 25(12), 6173–6183.
906 <https://doi.org/10.5194/hess-25-6173-2021>
- 907 Mohanty, B. P. (2013). Soil Hydraulic Property Estimation Using Remote Sensing: A Review.
908 *Vadose Zone Journal*, 12(4), vzj2013.06.0100. <https://doi.org/10.2136/vzj2013.06.0100>
- 909 Nakazato, M., & Ito, S. (2021). Geometrical aspects of entropy production in stochastic
910 thermodynamics based on Wasserstein distance. *Physical Review Research*, 3.
911 <https://doi.org/10.1103/PhysRevResearch.3.043093>
- 912 van Nes, E. H., Arani, B. M. S., Staal, A., van der Bolt, B., Flores, B. M., Bathiany, S., & Scheffer,
913 M. (2016). What Do You Mean, ‘Tipping Point’? *Trends in Ecology & Evolution*, 31(12),
914 902–904. <https://doi.org/10.1016/j.tree.2016.09.011>
- 915 Ouedraogo, F., Cherblanc, F., Naon, B., & Bénét, J.-C. (2013). Water transfer in soil at low water
916 content. Is the local equilibrium assumption still appropriate? *Journal of Hydrology*, 492,
917 117–127. <https://doi.org/10.1016/j.jhydrol.2013.04.004>
- 918 Perkins-Kirkpatrick, S. E., & Lewis, S. C. (2020). Increasing trends in regional heatwaves. *Nature*
919 *Communications*, 11(1), 3357. <https://doi.org/10.1038/s41467-020-16970-7>
- 920 Porada, P., Kleidon, A., & Schymanski, S. J. (2011). Entropy production of soil hydrological
921 processes and its maximisation. *Earth System Dynamics*, 2(2), 179–190.
922 <https://doi.org/10.5194/esd-2-179-2011>
- 923 Qian, H. (2006). Open-System Nonequilibrium Steady State: Statistical Thermodynamics,
924 Fluctuations, and Chemical Oscillations. *The Journal of Physical Chemistry B*, 110(31),
925 15063–15074. <https://doi.org/10.1021/jp061858z>
- 926 Running, Steve, Mu, Qiaozhen, Zhao, Maosheng, & Moreno, Alvaro. (2019). MOD16A2GF
927 MODIS/Terra Net Evapotranspiration Gap-Filled 8-Day L4 Global 500 m SIN Grid V006
928 [Data set]. NASA EOSDIS Land Processes DAAC.
929 <https://doi.org/10.5067/MODIS/MOD16A2GF.006>

- 930 Scheffer, M., Carpenter, S., Foley, J. A., Folke, C., & Walker, B. (2001). Catastrophic shifts in
931 ecosystems. *Nature*, *413*(6856), 591–596. <https://doi.org/10.1038/35098000>
- 932 Sehgal, V., & Mohanty, B. P. (2023). *Preferential Hydrologic States and Tipping Characteristics*
933 *of Global Surface Soil Moisture* (preprint). Preprints.
934 <https://doi.org/10.22541/essoar.167840001.13313960/v1>
- 935 Sehgal, V., Gaur, N., & Mohanty, B. P. (2021). Global Surface Soil Moisture Drydown Patterns.
936 *Water Resources Research*, *57*(1), e2020WR027588.
937 <https://doi.org/10.1029/2020WR027588>
- 938 Seneviratne, S. I., Lüthi, D., Litschi, M., & Schär, C. (2006). Land–atmosphere coupling and
939 climate change in Europe. *Nature*, *443*(7108), 205–209.
940 <https://doi.org/10.1038/nature05095>
- 941 Seneviratne, S. I., Corti, T., Davin, E. L., Hirschi, M., Jaeger, E. B., Lehner, I., et al. (2010).
942 Investigating soil moisture–climate interactions in a changing climate: A review. *Earth-*
943 *Science Reviews*, *99*(3), 125–161. <https://doi.org/10.1016/j.earscirev.2010.02.004>
- 944 Shokri, N., Lehmann, P., & Or, D. (2009). Critical evaluation of enhancement factors for vapor
945 transport through unsaturated porous media. *Water Resources Research*, *45*(10).
946 <https://doi.org/10.1029/2009WR007769>
- 947 Short Gianotti, D. J., Salvucci, G. D., Akbar, R., McColl, K. A., Cuenca, R., & Entekhabi, D. (2019).
948 Landscape Water Storage and Subsurface Correlation From Satellite Surface Soil
949 Moisture and Precipitation Observations. *Water Resources Research*, *55*(11), 9111–
950 9132. <https://doi.org/10.1029/2019WR025332>
- 951 Structure and Interpretation of Classical Mechanics. (n.d.). Retrieved June 15, 2023, from
952 <http://groups.csail.mit.edu/mac/users/gjs/6946/sicm-html/>
- 953 Sulla-Menashe, D., Gray, J. M., Abercrombie, S. P., & Friedl, M. A. (2019). Hierarchical mapping
954 of annual global land cover 2001 to present: The MODIS Collection 6 Land Cover product.
955 *Remote Sensing of Environment*, *222*, 183–194. <https://doi.org/10.1016/j.rse.2018.12.013>

- 956 Teuling, A. J., Seneviratne, S. I., Williams, C., & Troch, P. A. (2006). Observed timescales of
957 evapotranspiration response to soil moisture. *Geophysical Research Letters*, 33(23).
958 <https://doi.org/10.1029/2006GL028178>
- 959 Tuisku, P., Pernu, T. K., Tuomas K. Pernu, Tuomas K. Pernu, & Annala, A. (2009). In the light of
960 time. *Proceedings of The Royal Society A: Mathematical, Physical and Engineering*
961 *Sciences*, 465(2104), 1173–1198. <https://doi.org/10.1098/rspa.2008.0494>
- 962 Tuttle, S., & Salvucci, G. (2016). Empirical evidence of contrasting soil moisture–precipitation
963 feedbacks across the United States. *Science*, 352(6287), 825–828.
964 <https://doi.org/10.1126/science.aaa7185>
- 965 Van Vu, T., & Saito, K. (2022, December 13). Thermodynamic Unification of Optimal Transport:
966 Thermodynamic Uncertainty Relation, Minimum Dissipation, and Thermodynamic Speed
967 Limits. arXiv. <https://doi.org/10.48550/arXiv.2206.02684>
- 968 Verbesselt, J., Umlauf, N., Hirota, M., Holmgren, M., Van Nes, E. H., Herold, M., et al. (2016).
969 Remotely sensed resilience of tropical forests. *Nature Climate Change*, 6(11), 1028–1031.
970 <https://doi.org/10.1038/nclimate3108>
- 971 Vereecken, H., Kasteel, R., Vanderborght, J., & Harter, T. (2007). Upscaling Hydraulic Properties
972 and Soil Water Flow Processes in Heterogeneous Soils: A Review. *Vadose Zone Journal*,
973 6(1), 1–28. <https://doi.org/10.2136/vzj2006.0055>
- 974 Vereecken, Harry, Amelung, W., Bauke, S. L., Bogena, H., Brüggemann, N., Montzka, C., et al.
975 (2022). Soil hydrology in the Earth system. *Nature Reviews Earth & Environment*, 3(9),
976 573–587. <https://doi.org/10.1038/s43017-022-00324-6>
- 977 Wang, J., Salvucci, G. D., & Bras, R. L. (2004). An extremum principle of evaporation. *Water*
978 *Resources Research*, 40(9). <https://doi.org/10.1029/2004WR003087>
- 979 Wu, W., & Dickinson, R. E. (2004). Time Scales of Layered Soil Moisture Memory in the Context
980 of Land–Atmosphere Interaction. *Journal of Climate*, 17(14), 2752–2764.
981 [https://doi.org/10.1175/1520-0442\(2004\)017<2752:TSOLSM>2.0.CO;2](https://doi.org/10.1175/1520-0442(2004)017<2752:TSOLSM>2.0.CO;2)

982 Zhu, J., & Mohanty, B. P. (2002). Spatial Averaging of van Genuchten Hydraulic Parameters for
983 Steady-State Flow in Heterogeneous Soils: A Numerical Study. *Vadose Zone Journal*,
984 1(2), 261–272. <https://doi.org/10.2136/vzj2002.2610>
985